Scaling relations for heat and momentum transport in sheared Rayleigh–Bénard convection

Guru Sreevanshu Yerragolam[1,†], Christopher J. Howland[1], Richard J.A.M. Stevens[1], Roberto Verzicco[1,2,3], Olga Shishkina[4] and Detlef Lohse[1,4,†]

[1]Physics of Fluids Group, Max Planck Center for Complex Fluid Dynamics, J. M. Burgers Center for Fluid Dynamics, Department of Science and Technology, University of Twente, P.O. Box 217, 7500 AE Enschede, The Netherlands

[2]Dipartimento di Ingegneria Industriale, University of Rome "Tor Vergata", Via del Politecnico 1, Roma 00133, Italy

[3]Gran Sasso Science Institute, Viale F. Crispi, 7, 67100 L'Aquila, Italy

[4]Max Planck Institute for Dynamics and Self-Organization, Am Fassberg 17, 37077 Göttingen, Germany

(Received 16 February 2024; revised 8 July 2024; accepted 21 August 2024)

We provide scaling relations for the Nusselt number Nu and the friction coefficient C_S in sheared Rayleigh–Bénard convection, i.e. in Rayleigh–Bénard flow with Couette- or Poiseuille-type shear forcing, by extending the Grossmann & Lohse (*J. Fluid Mech.*, vol. 407, 2000, pp. 27–56, *Phys. Rev. Lett.*, vol. 86, 2001, pp. 3316–3319, *Phys. Rev. E*, vol. 66, 2002, 016305, *Phys. Fluids*, vol. 16, 2004, pp. 4462–4472) theory to sheared thermal convection. The control parameters for these systems are the Rayleigh number Ra, the Prandtl number Pr and the Reynolds number Re_S that characterises the strength of the imposed shear. By direct numerical simulations and theoretical considerations, we show that, in turbulent Rayleigh–Bénard convection, the friction coefficients associated with the applied shear and the shear generated by the large-scale convection rolls are both well described by Prandtl's (*Ergeb. Aerodyn. Vers. Gött.*, vol. 4, 1932, pp. 18–29) logarithmic friction law, suggesting some kind of universality between purely shear-driven flows and thermal convection. These scaling relations hold well for $10^6 \leq Ra \leq 10^8$, $0.5 \leq Pr \leq 5.0$, and $0 \leq Re_S \leq 10^4$.

Key words: turbulence simulation, turbulent convection

† Email addresses for correspondence: g.s.yerragolam@utwente.nl, d.lohse@utwente.nl

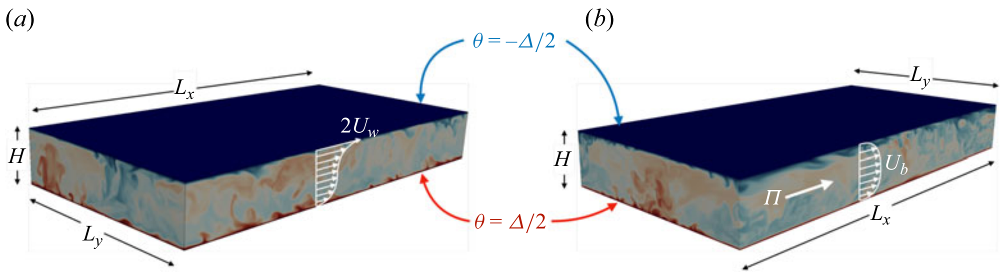

Figure 1. Schematic of the (*a*) CRB and (*b*) PRB systems.

1. Introduction

The interplay between buoyancy and shear in mixed thermal convection can be studied by either adding Couette-type forcing to the Rayleigh–Bénard (RB) system (Ahlers, Grossmann & Lohse 2009; Lohse & Xia 2010; Chilla & Schumacher 2012; Xia 2013; Shishkina 2021; Ahlers *et al.* 2022; Lohse & Shishkina 2023) to obtain the Couette–RB (CRB) system (Deardorff 1965; Ingersoll 1966; Hathaway & Somerville 1986; Domaradzki & Metcalfe 1988; Solomon & Gollub 1990; Shevkar *et al.* 2019; Blass *et al.* 2020, 2021), or by applying a Poiseuille-type forcing to obtain the Poiseuille–RB (PRB) system (Scagliarini, Gylfason & Toschi 2014; Zonta & Soldati 2014; Scagliarini *et al.* 2015; Pirozzoli *et al.* 2017). A schematic of the two systems is shown in figure 1.

The CRB and PRB systems are described by the incompressible Navier–Stokes equations, the continuity equation and the temperature transport equation, within the Boussinesq approximation. In Cartesian coordinates, they read

$$\partial_t u_i + u_j \partial_j u_i = -\rho^{-1} \partial_i p + \nu \partial_j^2 u_i + \beta g \delta_{i3} \theta + \Pi \delta_{i1}, \quad \partial_i u_i = 0, \tag{1.1a,b}$$

$$\partial_t \theta + u_j \partial_j \theta = \kappa \partial_j^2 \theta, \tag{1.2}$$

where $\boldsymbol{u} \equiv (u_x, u_y, u_z)$ is the velocity, p the pressure, θ the reduced temperature, ρ the density of the fluid, g the acceleration due to gravity antiparallel to the z direction, β the isobaric thermal expansion coefficient, ν the kinematic viscosity, κ the thermal diffusivity and H is the distance between the horizontal walls. At the top wall ($z = H$), the reduced temperature is set to $\theta = -\Delta/2$ while at the bottom wall ($z = 0$), the reduced temperature is set to $\theta = \Delta/2$. For the CRB system $\Pi = 0$, the bottom wall is at rest and a velocity of $2U_w$ is imposed on the top wall. For the PRB system, no-slip conditions are enforced at the walls and a volume forcing Π is applied in the streamwise direction such that it induces a bulk velocity of U_b averaged over the domain volume and time (for the details of the implementation of the shear forcing in the numerical simulations, we refer the reader to § 3). The streamwise direction is oriented along x and the spanwise direction along y. The aspect ratios of the system are defined by $\Gamma_x = L_x/H$ and $\Gamma_y = L_y/H$, with L_x, L_y being the dimensions of the system in the x and y directions, respectively.

The control parameters for the systems are the Rayleigh number, the Prandtl number and the Reynolds number associated with the shear forcing

$$Ra \equiv \frac{\beta g H^3 \Delta}{\nu \kappa}, \quad Pr \equiv \frac{\nu}{\kappa}, \quad Re_S \equiv \frac{U_S H}{\nu}. \tag{1.3a–c}$$

The characteristic velocity scale associated with the shear forcing U_S is given by $U_S \equiv U_w$ for the CRB system and $U_S \equiv U_b$ for the PRB system. Although U_b is formally a response parameter, in our numerical simulations the volume forcing term Π is computed at each time step to ensure a constant mass flow rate (Quadrio, Frohnapfel & Hasegawa 2016) dictated by U_b, making it a control parameter in our case. The shear forcing for the CRB system is given by the wall Reynolds number $Re_w \equiv U_w H/\nu$ whereas the shear forcing for the PRB system is given by the bulk Reynolds number $Re_b \equiv U_b H/\nu$. Henceforth, we use Re_S to indicate shear forcing in equations that are applicable to both CRB and PRB systems.

Similarly, one can also define a Reynolds number associated with the thermal forcing in these systems. From the input parameters, we can construct a Reynolds number $Re_F = U_F H/\nu \equiv \sqrt{Ra/Pr}$, using the free fall velocity scale $U_F = \sqrt{g\beta\Delta H}$. However, the free fall scale is often not a reliable estimate of the flow velocities that develop in natural convection flows. A more appropriate approach is to define the Reynolds number associated with the large-scale convection (LSC) roll given by $Re_L \equiv U_L H/\nu$, with U_L indicating the mean velocity of the 'wind of turbulence' generated by the LSC roll. The parameter Re_L is, however, a response parameter whose variation with Ra, Pr and Re_S is not known *a priori*.

In the limiting case of zero shear forcing, we can distinguish the Reynolds number associated with the LSC roll in pure RB flow as $Re_R(Ra, Pr) \equiv Re_L(Ra, Pr, Re_S = 0)$. The dynamics of the sheared RB systems are governed by a combined effect of both shear and thermal forcing. Therefore, we can also introduce the Reynolds number Re_T, which is constructed using the total velocity U_T comprising a vector sum of U_S and U_L. Naturally, the time-averaged wall shear stress τ_T generated by the total velocity U_T is also determined by the combined effect of τ_L, which is the time-averaged shear stress locally generated on the walls by the LSC roll, and τ_S, which is the mean streamwise shear stress generated on the walls due to the applied shear forcing. These shear stresses can be expressed in dimensionless form using the friction coefficients associated with the total shear, the LSC roll and the streamwise shear respectively, as

$$C_T \equiv \frac{2\tau_T}{\rho U_T^2}, \quad C_L \equiv \frac{2\tau_L}{\rho U_L^2}, \quad C_S \equiv \frac{2\tau_S}{\rho U_S^2}. \tag{1.4a–c}$$

Once again, in the limiting case of zero shear forcing, we can distinguish the friction coefficient associated with the LSC roll in pure RB flow as $C_R(Ra, Pr) \equiv C_L(Ra, Pr, Re_S = 0)$. The non-dimensional heat flux from the hot bottom wall to the cold top wall is given by the Nusselt number

$$Nu \equiv \frac{\langle u_z\theta - \kappa\partial_z\theta\rangle_{A,t}}{\kappa\Delta H^{-1}}, \tag{1.5}$$

with $\langle\rangle_{A,t}$ indicating the averaging in time and over any horizontal plane spanned by x and y. A summary of all response and control parameters discussed above is given in table 1 for reference. In this study, we are primarily interested in understanding the dependence of the response parameters on the control parameters, and the physics underlying the connections between the response parameters.

Using the exact relations for the global kinetic and thermal dissipation rates, Grossmann & Lohse (2000, 2001, 2002, 2004) offered a unifying theory for RB convection (hereafter referred to as the GL-theory). For cylinders of unit aspect ratio, Stevens *et al.* (2013) have demonstrated that fitting the GL-theory at four data points from Funfschilling *et al.* (2005) at $Ra = 2.96 \times 10^7$ and $Ra = 1.92 \times 10^{10}$ with $Pr = 4.38$, from Xia, Lam & Zhou (2002) at $Ra = 2.24 \times 10^8$ with $Pr = 554$ and from Kerr & Herring (2000) at $Ra = 10^7$ with $Pr = 0.07$ using four free parameters can predict Nu within 4 % of experimental and numerical results in most of the parameter space given by $10^4 \leq Ra \leq 10^{14}$ and $10^{-3} \leq$

Parameter	Definition	Type	Short description
Ra	$(\beta g H^3 \Delta)/(\nu\kappa)$	Control	Rayleigh number
Pr	ν/κ	Control	Prandtl number
Re_F	$U_F H/\nu \equiv \sqrt{Ra/Pr}$	Control	Reynolds number associated with free-fall velocity
Re_w	$U_w H/\nu$	Control	Wall Reynolds number for CRB system
Re_b	$U_b H/\nu$	Control	Bulk Reynolds number for PRB system
Re_S	$U_S H/\nu$	Control	Reynolds number associated with shear forcing
Re_L	$U_L H/\nu$	Response	Reynolds number associated with LSC rolls for sheared RB
Re_R	$U_R H/\nu \equiv Re_L(Re_S = 0)$	Response	Reynolds number associated with LSC rolls for pure RB ('wind Reynolds number')
Re_T	$U_T H/\nu$	Response	Reynolds number computed using the total velocity
C_S	$2\tau_S/(\rho U_S^2)$	Response	Friction coefficient associated with shear forcing
C_L	$2\tau_L/(\rho U_L^2)$	Response	Friction coefficient associated with LSC rolls for sheared RB
C_R	$2\tau_R/(\rho U_R^2) \equiv C_L(Re_S = 0)$	Response	Friction coefficient associated with LSC rolls for pure RB
C_T	$2\tau_T/(\rho U_T^2)$	Response	Friction coefficient computed using the total velocity
Nu	$\langle u_z\theta - \kappa\partial_z\theta\rangle_{A,t}/(\kappa\Delta H^{-1})$	Response	Nusselt number

Table 1. A summary of all control and response parameters discussed in § 1.

$Pr \leq 10^2$, with only two small ranges that exhibit a greater than 10 % disagreement. In the same paper Stevens *et al.* (2013), a fit of similar quality is achieved also for an aspect ratio $\varGamma = 1/2$, with slightly different prefactors. This work has further been extended by Ahlers *et al.* (2022) to include the effects of aspect ratios between 1/32 and 32. The GL-theory has also been extended to the ultimate regime (Grossmann & Lohse 2011), where the heat transport is considerably enhanced, as the laminar-type boundary layers become turbulent due to a non-normal–nonlinear instability; for a detailed discussion see Roche (2020) and Lohse & Shishkina (2023).

Presently, the GL-theory has been applied to RB convection without imposed shear. The objective of this work is to extend the theoretical approach to sheared thermal convection. Scagliarini *et al.* (2014, 2015); Pirozzoli *et al.* (2017); Blass *et al.* (2020, 2021) have made progress in understanding the variation of heat transfer in RB convection with imposed shear. Scagliarini *et al.* (2014, 2015) proposed a model based on the concept of eddy viscosity and eddy diffusivity to explain the counter-intuitive initial decrease and subsequent increase in Nu with increasing Re_b for the PRB system. Blass *et al.* (2020) observed a similar effect in the CRB system and attributed it to the initial destruction of the large-scale flow organisation and the subsequent formation of large meandering flow structures (Hutchins & Marusic 2007). They divided the flow into a buoyancy-dominated, a transitional and a shear-dominated regime, based on the Monin–Obukhov length scale. Blass *et al.* (2021) further investigated the effect of Pr on the variation of Nu with Re_w and concluded that the non-monotonic behaviour of $Nu(Re_w)$ is a consequence of flow layering, plume sweeping and bulk heat entrapment. Building on these findings, in this paper we propose a more general formulation applicable to sheared thermal convection, in the spirit of the GL-theory.

The objective of this paper is to extend the GL-theory to CRB and PRB systems by providing scaling relations for $Nu(Ra, Pr, Re_S)$ and $C_S(Ra, Pr, Re_S)$. Furthermore, we will show similarities in the dependence of C_S on Re_S in Couette and Poiseuille flows and C_L on Re_L in RB convection, suggesting some sort of universality in the behaviour of the friction coefficient in shear-driven flows and thermal convection. In § 2, we build the theoretical framework, using rigorous relations for globally averaged kinetic and thermal dissipation rates. In § 3, we validate the theoretical scaling relations against direct numerical simulations (DNS). Finally, the conclusions are presented in § 4.

2. Extending the Grossmann–Lohse theory to CRB and PRB

2.1. *Kinetic and thermal dissipation rates*

To extend the GL-theory to sheared thermal convection, we formulate exact global relations for the kinetic (ϵ_u) and thermal (ϵ_θ) dissipation rates in the CRB and PRB systems. These arise from the time- and volume-averaged equations for the kinetic energy and temperature variance, respectively. The relation for the mean thermal dissipation rate is the same as in the classical RB convection

$$\epsilon_\theta = \left\langle \kappa (\partial_j \theta)^2 \right\rangle_{V,t} = \kappa \frac{\Delta^2}{H^2} Nu, \tag{2.1}$$

see e.g. Shraiman & Siggia (1990) and Siggia (1994). The relation for the mean kinetic dissipation rate reads

$$\epsilon_u = \left\langle \nu (\partial_j u_i)^2 \right\rangle_{V,t} = \frac{\nu^3}{H^4} \left(\underbrace{(Nu-1) Ra Pr^{-2}}_{\text{Buoyancy term}} + \underbrace{C_S Re_S^3}_{\text{Shear term}} \right), \tag{2.2}$$

with $\langle \ldots \rangle_{V,t}$ indicating the average over time and volume. Note that the expression for thermal dissipation (2.1) is the same as that in classical RB convection but the expression for kinetic dissipation (2.2) includes contributions from both buoyancy and shear forcing.

2.2. *Kinetic energy, large-scale convection rolls and boundary layer thickness*

One of the central ideas of the GL-theory is the presence of persistent LSC rolls that churn the bulk of the system and generate boundary layers at the walls. As a result, the mean kinetic energy of the RB system is expected to scale as $\sim U_R^2$, where U_R is the velocity scale of the LSC roll (in the absence of any shear forcing). In pure RB flow, this mean kinetic energy is solely generated by the buoyancy forcing. However, in the case of sheared RB flow, where the LSC roll has a velocity scale U_L, the mean kinetic energy consists of contributions from both the LSC roll and the imposed shear flow. Therefore, we add the kinetic energy of the mean flow U_S^2 and the associated turbulent kinetic energy (TKE), which scales as the square of the friction velocity $u_\tau = \sqrt{\tau_S/\rho}$, to write

$$U_T^2 \approx U_L^2 + U_S^2 + 2\gamma u_\tau^2, \tag{2.3}$$

with γ being a prefactor. This can also be written in terms of the corresponding Reynolds numbers as

$$Re_T^2 \approx Re_L^2 + Re_S^2 + \gamma C_S Re_S^2. \tag{2.4}$$

For a laminar Prandtl–Blasius-type (Prandtl 1904; Blasius 1908) boundary layer, there is no TKE, so the contribution $C_S Re_S^2$ vanishes and we can approximate (2.4) as

$$Re_T^2 \approx Re_L^2 + Re_S^2. \tag{2.5}$$

An interpretation of the above equation (2.5) is that the velocity associated with the LSC roll is preferentially oriented along the direction orthogonal to the shear forcing, consistent with the flow structures observed by Pirozzoli *et al.* (2017); Blass *et al.* (2020). Note that the validity of (2.5) is limited to sufficiently low values of Re_S wherein the contribution to spanwise shear stresses from shear forcing is negligible in comparison with the contribution from the LSC rolls. At high shear forcing, the spanwise shear stresses generated by velocity fluctuations arising purely from shear forcing may no longer be negligible, in which case (2.5) no longer holds.

In the buoyancy-dominated regime, relation (2.5) can be better understood by considering many LSC rolls each orientated at an angle α with the streamwise direction and studying the probability distribution of α given by $\phi(\alpha)$. Here, we mean LSC rolls in a broad sense, without addressing the exact details of the flow organisation at this stage. Empirical observations regarding flow organisation are reported in section § 3.3. Since the total velocity U_T arises from a vector addition of the shear velocity and the LSC velocities, we can express it in terms of $\phi(\alpha)$ as

$$U_T^2 = \int_0^{2\pi} \phi(\alpha) \left(U_S^2 + U_L^2 + 2U_S U_L \cos(\alpha) \right) \mathrm{d}\alpha. \tag{2.6}$$

Due to the symmetry of the system and the periodic boundary conditions in the horizontal directions, it is reasonable to consider that there are an equal number of clockwise and counter-clockwise LSC rolls within the sheared RB system. When averaged over the entire volume of the system, we postulate that the probability distribution $\phi(\alpha)$ is symmetric about the spanwise direction, i.e. about $\alpha = \pm\pi/2$. Applying this symmetry condition to (2.6) gives us the relation (2.5). The velocity scale U_T associated with the kinetic energy of the system can thus be considered as a vector sum of perpendicular velocity contributions from the shear forcing in the streamwise direction and the LSC roll in the spanwise direction. Following this approach, we can also decompose the total shear stress τ_T generated by U_T into the streamwise component $\tau_s = \tau_T U_S/U_T$, generated by U_S, and the spanwise component $\tau_L = \tau_T U_L/U_T$, generated by U_L. This assumption gives us three equivalent definitions of the kinetic boundary layer thickness λ_u, namely

$$\lambda_u \equiv \frac{2H}{C_L Re_L} = \frac{2H}{C_S Re_S} = \frac{2H}{C_T Re_T}. \tag{2.7}$$

Here, we used the slope criterion from Shishkina *et al.* (2010) for the definition of the kinetic boundary layer thickness. Similarly, we define the thermal boundary layer thickness λ_θ also with the slope criterion as

$$\lambda_\theta \equiv \frac{H}{2Nu}. \tag{2.8}$$

2.3. *Estimating bulk and boundary layer contributions*

Another key idea of the GL-theory is the splitting of ϵ_u and ϵ_θ into their bulk and boundary layer contributions as follows:

$$\epsilon_u = \epsilon_{u,BL} + \epsilon_{u,bulk}, \quad \epsilon_\theta = \epsilon_{\theta,BL} + \epsilon_{\theta,bulk}, \tag{2.9a,b}$$

with $\epsilon_{u,BL}$ being the boundary layer contribution to the kinetic dissipation, $\epsilon_{u,bulk}$ being the bulk contribution to the kinetic dissipation, $\epsilon_{\theta,BL}$ being the boundary layer contribution to the thermal dissipation and $\epsilon_{\theta,bulk}$ being the bulk contribution to the thermal dissipation. Therefore, we focus on estimating $\epsilon_{u,BL}$, $\epsilon_{u,bulk}$, $\epsilon_{\theta,BL}$ and $\epsilon_{\theta,bulk}$ for sheared RB systems.

First, we estimate $\epsilon_{u,BL}$ using (2.7) as

$$\epsilon_{u,BL} \sim \nu \frac{U_T^2}{\lambda_u^2}\frac{\lambda_u}{H} \sim \frac{\nu^3}{H^4} C_T Re_T^3 \equiv \frac{\nu^3}{H^4}\left(\underbrace{C_L Re_L^3}_{\text{LSC term}} + \underbrace{C_S Re_S^3}_{\text{Shear term}}\right), \tag{2.10}$$

which is, in turn, a sum of contributions from the LSC rolls and the applied shear forcing. Note that the shear contribution here exactly matches that in the global relation (2.2). Next, we estimate $\epsilon_{u,bulk}$. Here, it is important to note that the bulk dissipation rate is dominated by the contribution from LSC rolls, while the contribution from applied shear forcing is much smaller. Therefore, we only focus on estimating the contribution to $\epsilon_{u,bulk}$ from the LSC rolls by assume that the velocity scale U_L associated with the LSC rolls is responsible for stirring the bulk with a kinetic energy that scales with U_L^2. However, LSC rolls are swept at the boundary layer height due to the applied shear forcing and the time scale of the stirring process is governed not by the velocity U_L associated with the LSC rolls but by U_T which is the total velocity scale. As we shall find later in § 3.2, this is a key assumption that explains the trend of Nu with increasing Re_S in the buoyancy-dominated regime. Following these assumptions, we write

$$\epsilon_{u,bulk} \sim U_L^2 \frac{U_T}{H} \equiv Re_L^2 Re_T. \tag{2.11}$$

At high-shear forcing, the contribution of the boundary layer to the dissipation rate arising from shear forcing dominates the bulk contribution from LSC rolls. In the limiting case of passive transport in Couette/Poiseuille flow, one can rigorously derive that the total kinetic dissipation rate $\epsilon_u = (\nu^3/H^4) C_S Re_S^3$. In this sense, the kinetic dissipation rate of sheared RB at high shear forcing will always be dominated by the boundary layer contribution and estimating $\epsilon_{u,bulk}$ in the shear-dominated regimes is redundant.

The analogous estimate for $\epsilon_{\theta,BL}$

$$\epsilon_{\theta,BL} \sim \kappa \frac{\Delta^2}{\lambda_\theta^2}\frac{\lambda_\theta}{H} \sim \kappa \frac{\Delta^2}{H^2} Nu, \tag{2.12}$$

is identical to the exact relation (2.1), on the one hand showing consistency of the approach, but on the other hand not giving new information. Therefore, following the GL-theory, we match the magnitude of the advective and diffusive terms of (1.2) at the thermal boundary layer height to obtain

$$u_y \partial_y \sim \kappa \partial_{zz}. \tag{2.13}$$

As in the GL-theory, for regimes where the thermal boundary layer is thicker than the kinetic boundary layer ($\lambda_\theta > \lambda_u$, associated with low Pr), we estimate $u_y \sim U_L$, $\partial_y \sim 1/H$, and $\partial_{zz} \sim \lambda_\theta^{-2}$. Using these estimates in (2.13) with λ_u from (2.7) and λ_θ from (2.8), we obtain

$$Nu \sim Pr^{1/2} Re_L^{1/2} \equiv \frac{Pr^{1/2}}{C_L Re_L^{1/2}} C_T Re_T. \tag{2.14}$$

For high Pr regimes, where $\lambda_\theta < \lambda_u$, we estimate $u_y \sim U_L \lambda_\theta / \lambda_u$ due to the fact that the relevant velocity scale at the thermal boundary height is smaller than the velocity U_L by a factor λ_θ/λ_u, exactly as in the GL-theory. Once again using the estimates $\partial_y \sim 1/H$, and $\partial_{zz} \sim \lambda_\theta^{-2}$ in (2.13) with λ_u from (2.7) and λ_θ from (2.8), we get

$$Nu \sim Pr^{1/3} Re_L^{1/3} (C_T Re_T)^{1/3} \equiv \frac{Pr^{1/3}}{C_L^{2/3} Re_L^{1/3}} C_T Re_T. \tag{2.15}$$

Also the bulk contribution to the thermal dissipation is estimated in an identical manner to the corresponding equation in the GL-theory, only with minor changes to reflect the new dependence on C_L, C_T and Re_T. For $\lambda_\theta > \lambda_u$

$$\epsilon_{\theta,bulk} \sim \Delta^2 \frac{U_L}{H} \sim \kappa \frac{\Delta^2}{H^2} Pr Re_L \equiv \kappa \frac{\Delta^2}{H^2} \frac{Pr}{C_L} (C_T Re_T), \tag{2.16}$$

and for $\lambda_\theta < \lambda_u$, where the relevant velocity scale is $U_L \lambda_\theta / \lambda_u$, we get

$$\epsilon_{\theta,bulk} \sim \Delta^2 \frac{U_L}{H} \frac{\lambda_\theta}{\lambda_u} \sim \kappa \frac{\Delta^2}{H^2} Pr C_L Re_L^2 Nu^{-1} \equiv \kappa \frac{\Delta^2}{H^2} \frac{Pr}{C_L} \frac{(C_T Re_T)^2}{Nu}. \tag{2.17}$$

We expect (2.14)–(2.17) to be valid in both buoyancy-dominated and shear-dominated regimes. This is accommodated by the fact that the dependencies $C_T(Re_T)$ and $C_L(Re_L)$ behave differently in the buoyancy-dominated and shear-dominated regimes. Compatibility of these relations in the limiting regimes is explained in the subsequent § 2.4.

2.4. *Limiting regimes*

It is important to note that there exist no pure power laws for Nu, Re_L and C_S as functions of Ra, Pr and Re_S. Nonetheless, it is useful to study the pure scaling power laws that arise from limiting regimes, in the interest of understanding the physics of the system. Based on the dominance of boundary layer and bulk contributions to the kinetic and thermal dissipation rates, the GL-theory provides four regimes *I*, *II*, *III* and *IV* for the pure RB system. Furthermore, each regime can be divided into two subregimes based on whether the thermal boundary layer is nested into the kinetic boundary layer or *vice versa*. We find that this classification of regimes is also applicable to buoyancy-dominated sheared RB. The phase space of Ra, Pr and Re_S is divided by four different transitions – (i) transition from boundary layer dominated regimes to bulk-dominated regimes, (ii) transition from buoyancy-dominated regime to shear-dominated regime, (iii) transition between regimes where the thermal boundary layer is nested inside the kinetic boundary layer or *vice versa* and (iv) transition from a laminar Prandtl–Blasius-type boundary layer to a turbulent Prandtl–von Kármán-type boundary layer.

It should also be noted that some of these limiting regimes may not exist for sheared RB in the shear-dominated state. For example, at high shear forcing, the shear term in $\epsilon_{u,BL}$ always dominates ϵ_u because shear forcing primarily increases the boundary layer contribution of the kinetic dissipation $(\nu^3/H^4)C_S Re_S^3$. Since the friction coefficient C_S associated with the applied shear can become independent of Re_S only asymptotically at infinite Re_S, shear-dominated systems with $\epsilon_u \sim \epsilon_{u,bulk}$ cannot exist.

We now proceed to first analyse the shear-dominated regime with $Re_S/Re_L \gg 1$. This can be realised in two ways – namely either Re_L is small or Re_L is not necessarily small but $Re_S \gg Re_L$. When Re_L is small, we assume the existence of a laminar Prandtl–Blasius-type boundary layer with

$$C_L \sim Re_L^{-1/2}, \tag{2.18}$$

which, along with (2.7) and (2.18), gives

$$C_S \sim Re_L^{1/2} Re_S^{-1}. \tag{2.19}$$

With the assumption (2.18), we see that (2.14) associated with small Pr becomes

$$Nu \sim Pr^{1/2} C_T Re_T, \tag{2.20}$$

and (2.15) associated with large Pr becomes

$$Nu \sim Pr^{1/3} C_T Re_T. \tag{2.21}$$

For the limiting case of $Re_L = 0$ one can see that relations (2.20) and (2.21) recover the scaling laws for passive transport in Couette (Yerragolam *et al.* 2022*a*) or Poiseuille flow (Kays & Crawford 1993) where the relation between C_T and Re_T depends on whether the kinetic boundary layer is laminar or turbulent. In the presence of a laminar boundary layer, the trivial scaling, $C_T \sim Re_T^{-1}$, applies. When the boundary layer turns turbulent with increased shear forcing, the relation between C_T and Re_T is given by Prandtl (1932) friction law obtained from the log-law mean velocity profile which states

$$\sqrt{\frac{2}{C_T}} = \frac{1}{k} \ln\left(Re_T \sqrt{\frac{C_T}{8}}\right) + B, \tag{2.22}$$

with $k \approx 0.41$ (Pirozzoli, Bernardini & Orlandi 2014) being the von Kármán (1934) constant and $B \approx 5$ (Pirozzoli *et al.* 2014) indicating the log-law intercept.

When Re_L is not necessarily small and $Re_S \gg Re_L$, we consider that the passive transport relations of (2.20) or (2.21) remain relevant, and that the dependence of $C_T(Re_T)$ is unchanged to that described above. For this case of larger Re_L, we assume that the thermal dissipation is dominated by contributions from the bulk, so that the global dissipation relation (2.1) can be estimated by (2.16) or (2.17). When we compare the passive transport relations with the dissipation estimates, we find that C_L must become independent of Re_L, with $C_L \sim Pr^{1/2}$ for low Pr and $C_L \sim Pr^{1/3}$ for high Pr. Furthermore, the behaviour of Re_L in these cases can be revealed by combining the passive transport relations (2.20) or (2.21) with the boundary-layer estimate for the kinetic dissipation rate (2.10). For low Pr this produces $Re_L \sim Ra^{1/2} Pr^{-3/4}$, and for high Pr we get $Re_L \sim Ra^{1/2} Pr^{-5/6}$, which exactly match the Reynolds number scaling relations found in the boundary layer dominated regime I of the GL-theory for classical RB convection.

Now, we focus on the buoyancy-dominated regimes where $Re_S/Re_L \lesssim 1$ and $C_S Re_S^3 \ll (Nu-1) Ra Pr^{-2}$ such that the shear contribution to the kinetic dissipation can be neglected in comparison with the buoyancy contribution. With this restriction, we

Regime	ϵ_u	ϵ_θ	BL ratio	Nu/Nu_R	Re_L/Re_R
I_l	BL (2.24)	BL (2.14)	$\lambda_\theta > \lambda_u$	$(C_L^2 Re_L)^{-1/8}$	$(C_L^2 Re_L)^{-1/4}$
I_u	BL (2.24)	BL (2.15)	$\lambda_\theta < \lambda_u$	$(C_L^2 Re_L)^{1/12}$	$(C_L^2 Re_L)^{-1/6}$
II_l	bulk (2.11)	BL (2.14)	$\lambda_\theta > \lambda_u$	$(Re_T/Re_L)^{-1/5}$	$(Re_T/Re_L)^{-2/5}$
II_u	bulk (2.11)	BL (2.15)	$\lambda_\theta < \lambda_u$	$(C_L^2 Re_L)^{1/5}(Re_T/Re_L)^{-1/5}$	$(C_L^2 Re_L)^{1/5}(Re_T/Re_L)^{-2/5}$
III_l	BL (2.24)	bulk (2.16)	$\lambda_\theta > \lambda_u$	$(C_L^2 Re_L)^{-1/3}$	$(C_L^2 Re_L)^{-1/3}$
III_u	BL (2.24)	bulk (2.17)	$\lambda_\theta < \lambda_u$	$(C_L^2 Re_L)^{1/7}$	$(C_L^2 Re_L)^{-1/7}$
IV_l	bulk (2.11)	bulk (2.16)	$\lambda_\theta > \lambda_u$	$(Re_T/Re_L)^{-1/2}$	$(Re_T/Re_L)^{-1/2}$
IV_u	bulk (2.11)	bulk (2.17)	$\lambda_\theta < \lambda_u$	$(C_L^2 Re_L)^{1/3}(Re_T/Re_L)^{-1/3}$	$(C_L^2 Re_L)^{1/9}(Re_T/Re_L)^{-4/9}$

Table 2. Scaling relations for the Nusselt number Nu and LSC Reynolds number Re_L in the buoyancy-dominated regime of sheared RB convection with a laminar Prandtl–Blasius-type boundary layer. The first column indicates the GL regime, the second column indicates the bulk or boundary layer (BL) dominance of the kinetic dissipation rate with the applicable scaling estimate in the parenthesis and the third column indicates the bulk or BL dominance of the thermal dissipation rate with the applicable scaling estimate in the parenthesis. The fourth column indicates whether the kinetic BL is thicker than the thermal boundary layer or *vice versa*. The fourth and fifth columns indicate the scaling relations for Nu/Nu_R and Re_L/Re_R using the values of Nu and Re_R estimated for the pure RB system from GL-theory.

approximate (2.2) as

$$\epsilon_u \approx \frac{\nu^3}{H^4}(Nu - 1)RaPr^{-2}, \tag{2.23}$$

and (2.10) as

$$\epsilon_{u,BL} \approx \frac{\nu^3}{H^4} C_L Re_L^3. \tag{2.24}$$

Using these approximations, we can provide scaling relations between Nu/Nu_R and Re/Re_R for buoyancy-dominated sheared RB system with Nu_R and Re_R being the Nusselt number and Reynolds number associated with the LSC rolls for the pure RB system. Following the GL-theory, there are various regimes that can be relevant depending on whether the dissipation rates are dominated by boundary layer or bulk contributions, and whether the thermal BL is thicker than the kinetic BL. For each of these regimes, we combine (2.7) and (2.23) with the relevant estimates for the dominant dissipation rate contribution to give expressions for $Nu(Ra, Pr, C_L, Re_L, Re_T)$ and $Re_L(Ra, Pr, C_L, Re_L, Re_T)$. Since our approach is consistent with the GL-theory, the Ra and Pr dependence simply recovers the scaling relations $Nu_R(Ra, Pr)$ and $Re_R(Ra, Pr)$ found for the various regimes of pure RB, providing us with scaling relations for Nu/Nu_R and Re_L/Re_R that only depend on C_L, Re_L and Re_T. In table 2, we outline the relevant estimates for the dissipation rates and present the resulting scaling relations. Is it important to note that these scaling relations are only applicable to buoyancy-dominated sheared RB flows with scaling-wise laminar Prandtl–Blasius-type BLs.

In the buoyancy-dominated classical GL regimes, we can consider the Prandtl–Blasius scaling (2.18) to hold for small shear forcing (i.e. $Re_S \lesssim Re_L$). With this assumption, $C_L^2 Re_L \approx 1$, so the values of Nu and Re_L remain unchanged for buoyancy-dominated regimes I and III, whereas for buoyancy-dominated regimes II and IV, the non-monotonic behaviour of Nu with increasing Re_S becomes apparent. Although Nu seems to decrease with increasing Re_S in the buoyancy-dominant II and IV regimes, it is important to note that this behaviour is subject to the condition that the BL is a laminar one of the Prandtl–Blasius type. If the BL becomes turbulent, the expected decrease in Nu in the buoyancy-dominated regime might disappear. In this study, we will explore the Nu response in the buoyancy-dominated II_u regime where we can still observe the decrease in Nu with increasing Re_S within reasonable computational cost.

3. Results from the direct numerical simulations

3.1. *Scheme and procedure*

In this section, we will compare the scaling relations derived in the previous section against the results from our DNS. Equations (1.1*a*,*b*) and (1.2) are solved numerically using the in-house open-source code 'AFiD', which is based on a second-order finite-difference scheme (van der Poel *et al.* 2015). The code has been extensively validated (Verzicco & Orlandi 1996; Verzicco & Camussi 1997; Stevens, Verzicco & Lohse 2010; Stevens, Lohse & Verzicco 2011; Kooij *et al.* 2018). We impose periodic boundary conditions in the horizontal directions and no-slip boundary conditions at the top and bottom walls. For most simulations, we use domains of aspect ratios $\varGamma_x = 8$ and $\varGamma_y = 4$. We also performed CRB simulations with $\varGamma_x = 48$ and $\varGamma_y = 24$ for $Ra = 10^7$, $Pr = 1$ to study large-scale flow structures. Due to the need for high resolution at large Ra, the RB simulations for $Ra = 10^{10}$, $Pr = 1$ and $Ra = 10^{11}$, $Pr = 1$ were performed in domains of aspect ratios $\varGamma_x = \varGamma_y = 4$, while the RB simulation for $Ra = 10^{12}$, $Pr = 1$ was performed in domain of aspect ratios $\varGamma_x = \varGamma_y = 2$. For the CRB simulations, the wall velocities $(-U_w)$ and U_w were imposed as Dirichlet boundary conditions on the bottom and top walls, respectively. This is done for numerical reasons (Bernardini *et al.* 2013) and does not affect the analysis of the results. The equivalent velocity fields of the CRB system with the bottom wall at rest and the top wall at $2U_w$ can be obtained by a simple Galilean transformation, i.e. by adding U_w to the numerically obtained flow field. For the PRB simulations, the volume forcing term $\varPi$ is computed at each time step to ensure a constant mass flow rate (Quadrio *et al.* 2016).

We use a uniform discretisation in the horizontal, periodic directions and a non-uniform grid in the wall-normal direction, in which we employ higher grid resolution in the BLs next to the walls. The thermal BL was ensured to be sufficiently resolved according to the resolution requirements put forward by Shishkina *et al.* (2010). The near-wall resolution is comparable to that of Lozano-Durán & Jiménez (2014); Pirozzoli *et al.* (2014); Lee & Moser (2018) to ensure that the kinetic BL is sufficiently resolved. The simulations were run for a long enough physical time for the standard deviation of Nu to converge within approximately 1 % of its mean value. In our previous work (Yerragolam *et al.* 2022*b*), we verified that the Nu and Re_τ obtained from a domain with $\varGamma_x = 8$ and $\varGamma_y = 4$ shows a difference of less than 1 % from the Nu obtained from a domain with $\varGamma_x = 48$ and $\varGamma_y = 24$. This observation is also supported by the fact that Nu for the RB system converges at an approximate aspect ratio $\varGamma_x = \varGamma_y = 4$ (Stevens *et al.* 2018).

Since many of the scaling relations in § 2.4 rely on the value of the wind Reynolds number Re_R, obtaining an estimate for Re_R from the numerical simulations of pure RB is necessary. The value of Re_R can be estimated in two possible ways. The first estimate can be obtained by using $Re_{max} = U_{max}H/\nu$ where U_{max} is the maximum value of the root mean squared (r.m.s.) horizontal velocity profile $u_R(z) \equiv \sqrt{\langle u_x^2 + u_y^2\rangle_{A,t}}$ at a height $z = \delta$ as shown in figure 2(*a*). The second estimate can be obtained by using the global r.m.s. velocity $Re_{rms} = U_{rms}H/\nu$ with $U_{rms} \equiv \sqrt{\langle u_x^2 + u_y^2 + u_z^2\rangle_{V,t}}$. In figure 2(*b*) and 2(*c*), we can see that these estimates are almost identical, providing strong evidence that the LSC

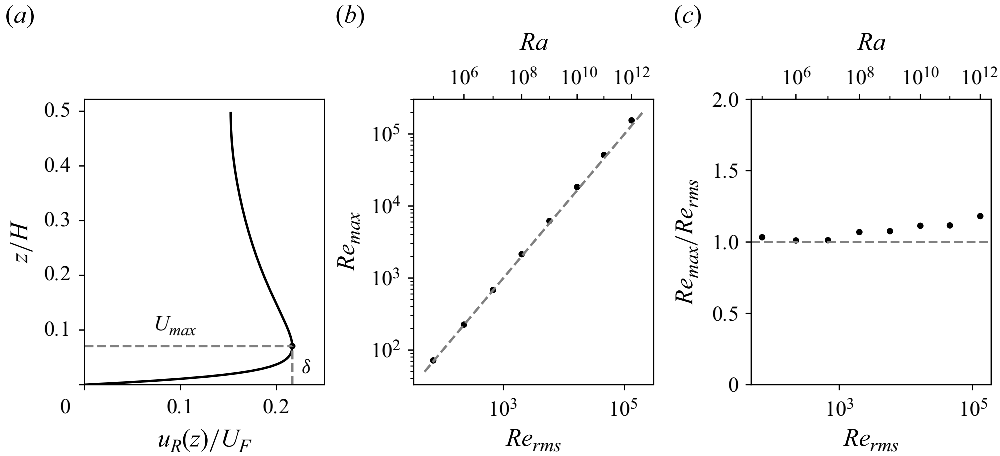

Figure 2. (a) The r.m.s. horizontal velocity profile $u_R(z)$ normalised with the free-fall velocity for RB system with $Ra = 10^7$, $Pr = 1.0$ is shown as a function of wall-normal height z, indicating the maximum value U_{max} occurring at a wall-normal height δ. (b) Value of Re_{max} obtained from U_{max} is plotted against the globally averaged r.m.s. velocity Re_R of the RB system. The dashed grey line indicates $Re_{max} = Re_{rms}$, showing that these two estimates are virtually identical. (c) Re_{max} compensated with Re_{rms} plotted against Re_{rms}, once again emphasising that the two estimates are equivalent within the 5 decades of Ra and nearly 3 decades of Re_{rms} investigated here. The values of Ra are shown on the top for reference. This figure is also available at https://www.cambridge.org/S0022112024008723/JFM-Notebooks/files/figure2.

rolls driving the wind at the wall also provide the dominant contribution to the mean kinetic energy in RB convection. In all the results discussed henceforth, we adopt Re_{rms} as an estimate for Re_R. Unlike in Couette or Poiseuille flow, the mean shear stress at the wall is zero in RB convection. However, we can use the mean gradient of the r.m.s. horizontal velocity $\langle \partial_z u_R(z)\rangle_{W,t}$ to calculate the friction coefficient C_R associated with the large-scale circulation. Here, $\langle \cdots \rangle_{W,t}$ indicates time averaging over the surface of the walls. The variation of C_R with Re_R is discussed separately in § 3.5.

3.2. *Global response parameters*

We now validate the scaling relations for Nu and C_S derived in § 2.4. Within the parameter range of Ra, Pr and Re simulated, we already observe multiple transitions. As shear forcing is increased, we undergo transition from the buoyancy-dominated regime to the shear-dominated regime. For low shear forcing, $\epsilon_u \sim \epsilon_{u,bulk}$ with $\lambda_\theta < \lambda_u$ whereas for high shear forcing, $\epsilon_u \sim \epsilon_{u,BL}$ with $\lambda_\theta/\lambda_u \sim Pr^{1/2}$ (Yerragolam *et al.* 2022*a*). Additionally, at low shear forcing, we observe a laminar Prandtl–Blasius-type BL which undergoes a transition into a turbulent one at high shear.

In the buoyancy-dominated regime, we assume the presence of Prandtl–Blasius-type kinetic boundary layer with the friction coefficient C_L given by (2.18). For the parameter range of our simulations, the relevant convection regime is II_u, so combining the relevant relation from table 2 with (2.18), we arrive at

$$\frac{Nu}{Nu_R} \sim \left(\frac{Re_T}{Re_L}\right)^{-1/5}. \tag{3.1}$$

In the buoyancy-dominated regimes, we also take (2.19) for the friction coefficient C_S associated with the imposed shear. In order to further simplify these equations, we approximate $Re_L \approx Re_R$ in the buoyancy-dominated regime, which is justified by the weak variation of Re_L with increasing Re_S in (table 2). With this assumption, we can rewrite (2.19) as

$$C_S \sim \sqrt{Re_R}/Re_S, \tag{3.2}$$

and use (2.5) to rewrite (3.1) as

$$Nu/Nu_R \sim \left(\sqrt{1 + \left(Re_S^2/Re_R^2\right)}\right)^{-1/5}. \tag{3.3}$$

These equations show good agreement with the numerical data plotted in figures 3(*a*)–3(*d*) for the buoyancy-dominated regime. Note that (3.1) and (3.3) do not explicitly state the dependence of $Nu_R(Ra, Pr)$ or $Re_R(Ra, Pr)$. There is no pure scaling exponent for $Nu_R(Ra)$ in pure RB for regime II_u. The values of Nu_R and Re_R used for figures 3(*b*) and 3(*d*) are obtained from numerical simulations of pure RB. The present extension to the GL-theory assumes that the values of Nu_R and Re_R are known *a priori*, and only attempts to provide scaling relations for the normalised quantities $Nu/Nu_R(Re_S/Re_R)$ and $C_S/C_R(Re_S/Re_R)$ in the buoyancy-dominated regime.

For the shear-dominated regime, we observe that the BL becomes turbulent. In this case, (2.19) is no longer valid. Instead, the relation between C_T and Re_T is given by (2.22). Note that, in the limiting case of very high-shear forcing, $Re_T \approx Re_S$. Equation (2.22) can be rewritten as

$$\sqrt{\frac{2}{C_S}} = \frac{1}{k}\ln\left(Re_S\sqrt{\frac{C_S}{8}}\right) + B, \tag{3.4}$$

and (2.20) can be rewritten using (2.7) as

$$Nu \sim Pr^{1/2} C_S Re_S, \tag{3.5}$$

which agrees well with the numerical data points in figures 3(*c*) and 3(*d*) at very high shear forcing. However, it is more useful to substitute the value of C_T obtained from (2.22) into (2.20) and approximate Re_T from (2.5) as

$$Re_T \approx \sqrt{Re_R^2 + Re_S^2}, \tag{3.6}$$

to obtain the dashed lines plotted in figure 3(*a*), which show better agreement for a larger range of Re_S/Re_R in the shear-dominated regime. The approximation given by (3.6) is then validated in figure 4(*a*). The additional energy term $\gamma C_S Re_S^2$ from (2.4) that corresponds to the turbulent fluctuations arising from shear forcing is shown in figure 4(*b*) with the value of the prefactor $\gamma \approx 10.24$. Note that the contribution from the fluctuations is much smaller than the contribution from the mean streamwise velocity, thereby making (3.6) a good approximation.

3.3. *Large-scale convection rolls*

Next, we confirm the theoretical assumptions on the LSC rolls made in § 2.2. The three-dimensional volume visualisation in figure 5 shows the streamlines associated with these LSC rolls and it can be seen that they are predominantly oriented in the spanwise direction. However, the large-scale temperature structures in figure 5 are seen to be aligned neither fully along the streamwise direction, nor fully along the spanwise direction but along a diagonal. The thermal plumes that comprise these large-scale structures experience

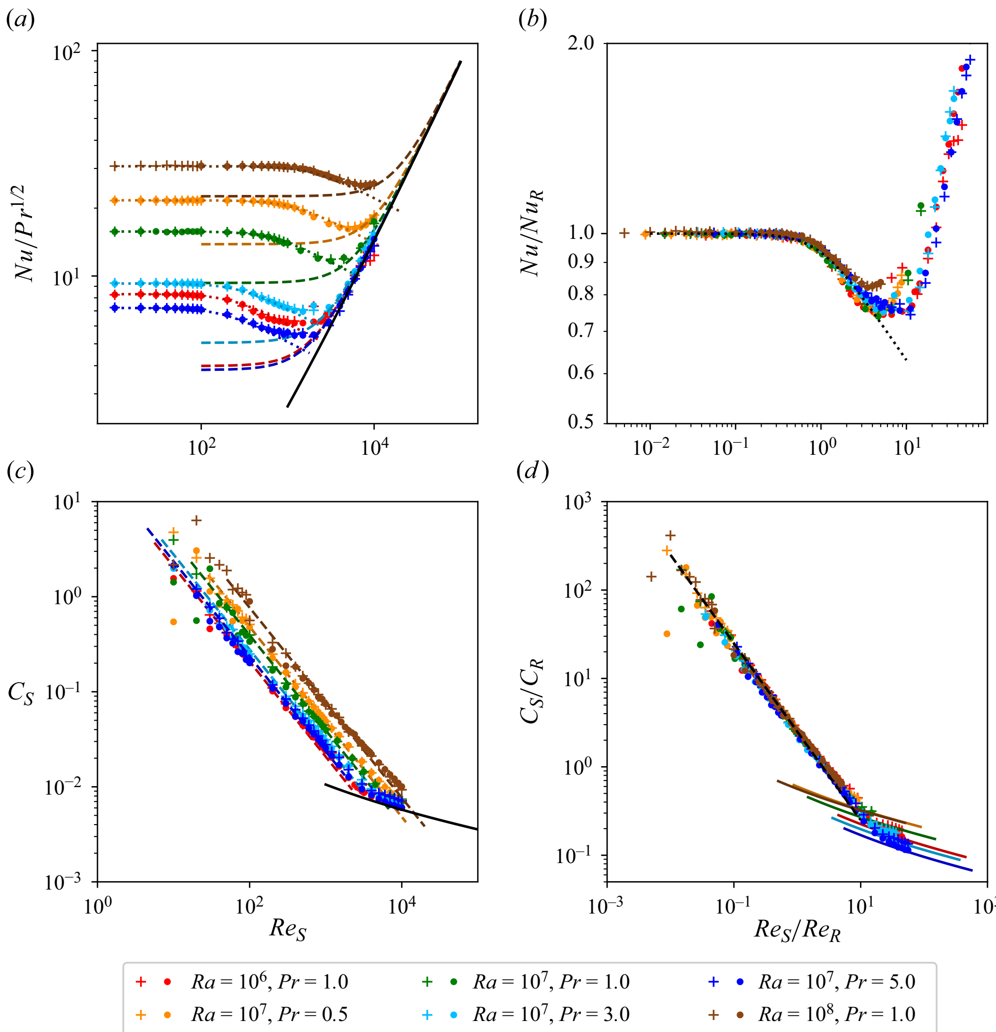

Figure 3. (*a*) Value of $Nu/Pr^{1/2}$ plotted against Re_S. The black solid line indicates (3.5), the dashed lines indicate (2.20) and the dotted lines indicate (3.3). (*b*) Value of Nu/Nu_R plotted against Re_S/Re_R. Dotted lines indicate (3.3). (*c*) Value of C_S plotted against Re_S. The black solid line indicates (3.4) and coloured dashed lines indicate (2.19). (*d*) Value of C_S normalised with C_R plotted against Re_S/Re_R. Coloured dashed lines indicate (3.4) and black dashed line indicates (2.19). The data for PRB are indicated with plus markers and the data for CRB are indicated with dot markers. This figure is also available at https://www.cambridge.org/S0022112024008723/JFM-Notebooks/files/figure3.

the advective effects of both U_L in the spanwise direction and U_S in the streamwise direction. Therefore, the orientation of these large scale temperature flow structures in the x–y plane is tilted along a diagonal whose slope is approximately given by U_L/U_S. This is made clearer in figure 6 through the visualisation of the non-dimensional time-averaged local shear stress $\boldsymbol{\tau}'_w \equiv (\tau'_x, \tau'_y, 0)$ computed at the bottom wall in the large aspect ratio CRB system by subtracting the wall-averaged streamwise shear stress in the following way:

$$\tau'_x = HU_F^{-1} \left\langle \partial_z u_x - \langle \partial_z u_x \rangle_{x,y,t} \right\rangle_t, \quad \tau'_y = HU_F^{-1} \left\langle \partial_z u_y \right\rangle_t. \qquad (3.7a,b)$$

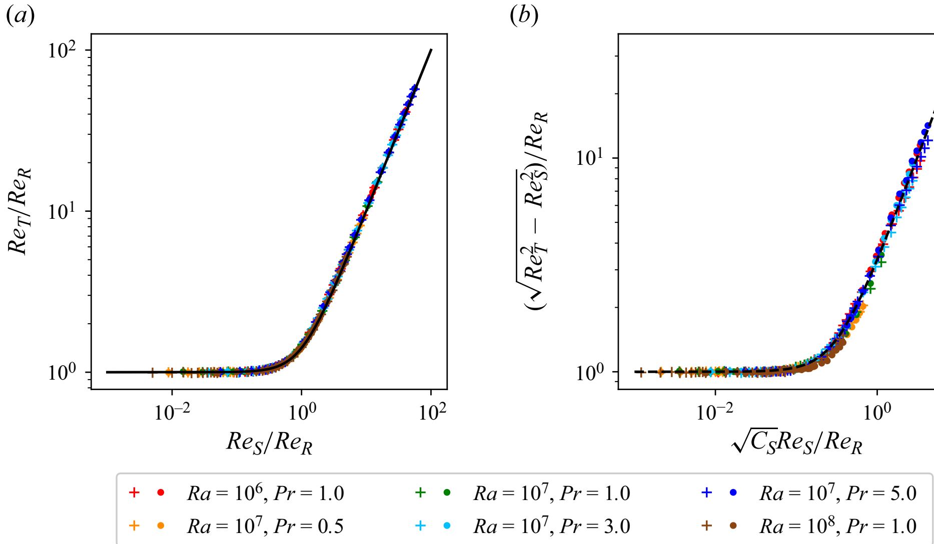

Figure 4. (*a*) Value of Re_T/Re_R plotted against Re_S/Re_R. The black solid line indicates the relation (2.5). (*b*) Value of $(\sqrt{Re_T^2 - Re_S^2})/Re_R$ plotted against $\sqrt{C_S}Re_S/Re_R$. The black dashed line indicates the relation (2.4) with $\gamma \approx 10.24$. The data for PRB are indicated with plus markers and the data for CRB are indicated with dot markers. This figure is also available at https://www.cambridge.org/S0022112024008723/JFM-Notebooks/files/figure4.

Figure 6(*a*) shows the wall shear for the RB system i.e. for $Re_w = 0$ and the zoomed inset in figure 6(*b*) shows the vectors of $\boldsymbol{\tau}_w'$. As expected, the LSC rolls are randomly oriented and no global alignment of $\boldsymbol{\tau}_w'$ is observed. A visual inspection of figures 6(*c*), 6(*e*) and 6(*g*) reveals that the large-scale flow structures seem to be oriented along the diagonal whose slope is approximately given by Re_R/Re_w. However, figures 6(*d*), 6(*f*) and 6(*h*) show that $\boldsymbol{\tau}_w'$ is primarily oriented along the spanwise direction in the transitional regime. Figure 6(*i*) shows the breakdown of the LSC rolls and the formation of large meandering flow structures (Hutchins & Marusic 2007; Blass *et al.* 2020, 2021) in the shear-dominated regime, while figure 6(*j*) shows that $\boldsymbol{\tau}_w'$ is predominantly aligned in the streamwise direction in the shear-dominated regime.

For further confirmation of the changes in the LSC rolls, we study the probability distribution function $\phi(\alpha)$ of the angle α spanned by the horizontal velocity component fluctuations $\boldsymbol{u_h'} \equiv (u_x', u_y', 0)$ with the streamwise direction x. In figures 7(*a*)–7(*e*) it can be seen that the behaviour of $\phi(\alpha)$ is qualitatively quite similar for the CRB and PRB systems. In the RB system, the LSC rolls are randomly oriented as shown by a uniform $\phi(\alpha)$ in figure 7(*a*). In the buoyancy-dominated regime, the LSC roll has a strong tendency to align in the spanwise directions in the transitional regime, as shown in figures 7(*b*) and 7(*d*). In the shear-dominated regime, the velocity fluctuations are predominantly aligned in the streamwise direction as in the case of turbulent Couette/Poiseuille flows, as seen in figures 7(*c*) and 7(*e*). At the thermal BL height, the symmetry of $\phi(\alpha)$ about $\alpha = \pm\pi/2$ is strongly suggested for all three regimes by the data from the numerical simulations as shown in figures 7(*f*)–7(*h*), confirming the assumption made in (2.6). In figure 7(*f*), the small non-uniformity in $\phi(\alpha)$ is attributed to the numerical confinement experienced by the flow structures in domains of a smaller aspect ratio of $\varGamma_x = 8$ and $\varGamma_y = 4$. For the relatively unconfined case with $\varGamma_x = 48$ and $\varGamma_y = 24$, the probability distribution is nearly uniform for all values of α.

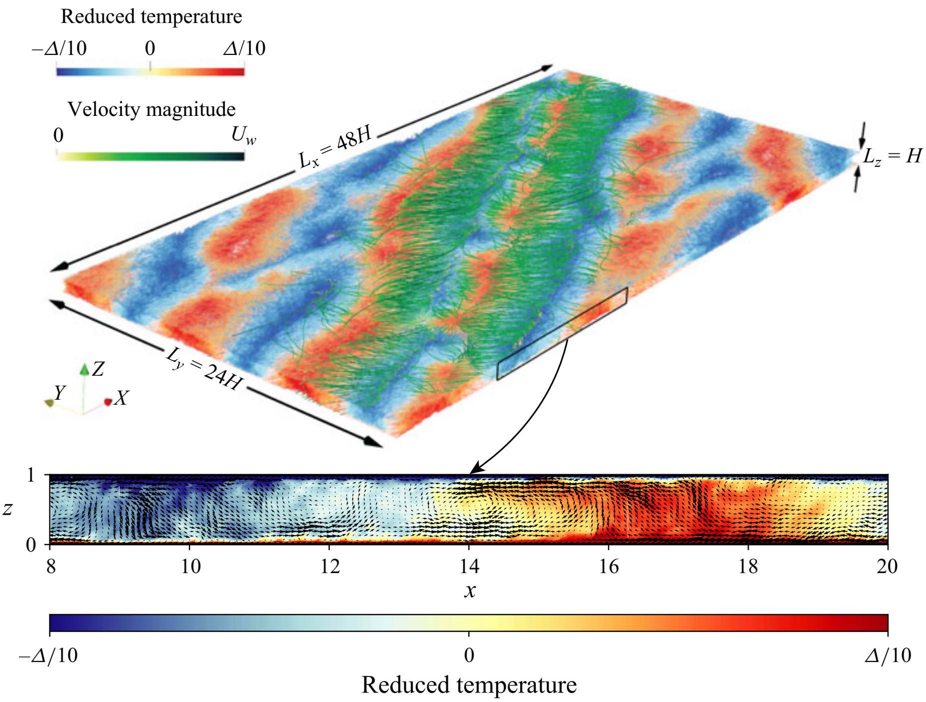

Figure 5. Three-dimensional volume visualisation of the time-averaged reduced temperature field of a CRB system with $Ra = 10^7$, $Pr = 1.0$, $Re_w = 1414$, $\Gamma_x = 48$, $\Gamma_y = 24$ with the averaging time being 100 free-fall time units. The green curves indicate the streamlines of the time-averaged velocity field $\langle \boldsymbol{u} \rangle_t - U_w \hat{x}$. The spanwise reorientation and streamwise sweeping of the plumes are evident. The zoomed inset shows the time-averaged two-dimensional visualisation of the temperature and velocity vectors in the x–z plane. The plumes carry streamwise momentum along with temperature and are swept in the streamwise direction, causing a reduction in the heat transport.

3.4. *Dissipation rates*

We now investigate the bulk and BL contributions to the global kinetic and thermal dissipation rates described in § 2.1. We validate the rigorous relations given by (2.1) and (2.2) using the data obtained from numerical simulations as shown in figures 8(*a*) and 8(*b*), respectively. For the range of Ra and Pr studied in this work, as long as the flow is buoyancy dominated, the system is in the II_u regime with $\epsilon_u \sim \epsilon_{u,bulk}$. With increasing shear forcing, the shear term of (2.2) increases the BL contribution of the kinetic dissipation due to the formation of streamwise velocity gradients close to the wall. For sufficiently strong shear, the kinetic dissipation will be dominated by the BL contribution with $\epsilon_u \sim \epsilon_{u,BL}$ as shown in 8(*c*). On the contrary, figure 8(*d*) shows that the thermal dissipation rate is dominated by the BL contribution for the entire range of Re_S considered in this study but the contribution reduces noticeably towards higher Re_S. For extremely strong shear, a possibility of a transition towards bulk dominance in thermal dissipation cannot be ruled out.

3.5. *Friction coefficient in Rayleigh–Bénard flow*

So far, we have considered only the laminar Prandtl–Blasius-type kinetic BLs in the buoyancy-dominated regime with the BL only becoming turbulent in highly

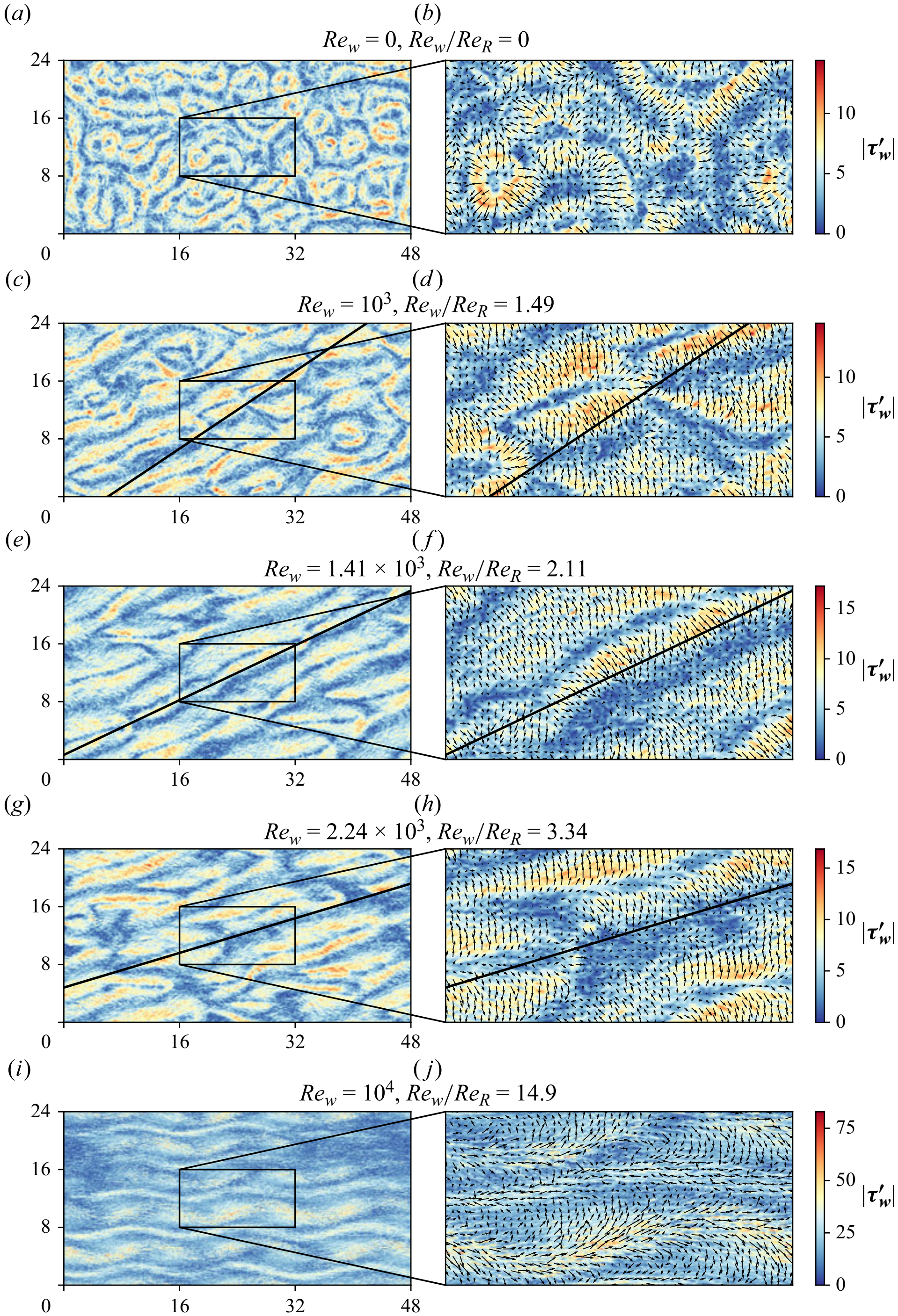

Figure 6. Visualisation of $\boldsymbol{\tau}'_w$ for the CRB system with $Ra = 10^7$ and $Pr = 1$. Panels (*c*), (*e*) and (*g*) are in the buoyancy-dominated regime and panel (*i*) is in the shear-dominated regime. The colour bars indicate the magnitude of $\boldsymbol{\tau}'_w$ while the black arrows in the magnified panels (*b*), (*d*), (*f*), (*h*) and (*j*) indicate the direction of $\boldsymbol{\tau}'_w$. The black lines in (*c*–*h*) indicate the slope of $(Re_w/Re_R)^{-1}$. This figure is also available at https://www.cambridge.org/S0022112024008723/JFM-Notebooks/files/figure6.

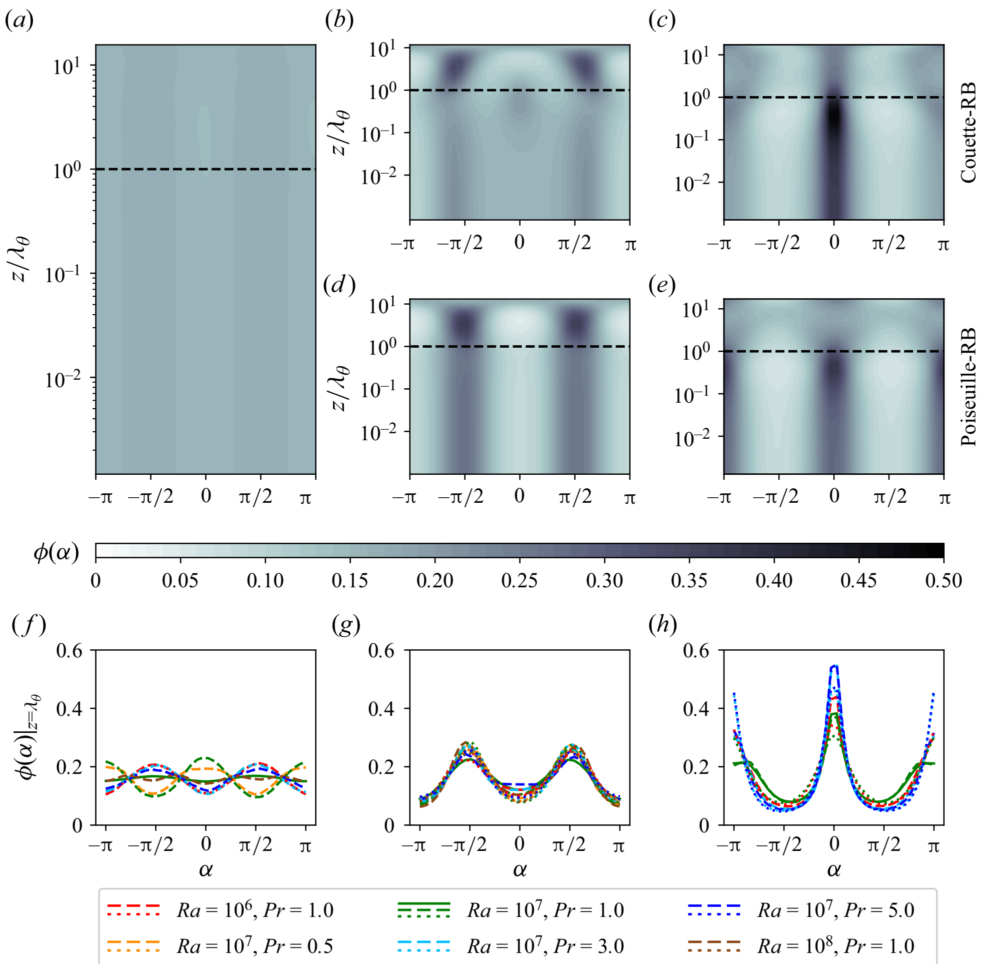

Figure 7. The probability distribution $\phi(\alpha)$ of the flow orientation angle α for all heights $0 \leq z/\lambda_\theta \leq Nu$ for $Ra = 10^7$, $Pr = 1$, $\Gamma_x = 48$ and $\Gamma_y = 24$ in (*a*) RB flow (i.e. with $Re_S = 0$), (*b*,*d*) buoyancy-dominated regime with $Re_S/Re_R \approx 2.11$ and (*c*,*e*) shear-dominated regime with $Re_S/Re_R \geq 10$. Panels (*b*,*c*) are for the CRB system while panels (*d*,*e*) are for the PRB system. The black dashed lines indicate the height of the thermal BL and the colour bar indicates the magnitude of the probability. The probability distribution $\phi(\alpha)$ at the thermal BL height plotted against angle α for various Ra and Pr in (*f*) RB flow, (*g*) buoyancy-dominated regime and (*h*) shear-dominated regime. The solid lines are the CRB system with $\Gamma_x = 48$ and $\Gamma_y = 24$, the dashed lines are for the CRB system with $\Gamma_x = 8$ and $\Gamma_y = 4$ and the dotted lines are for the PRB system with $\Gamma_x = 8$ and $\Gamma_y = 4$. This figure is also available at https://www.cambridge.org/S0022112024008723/JFM-Notebooks/files/figure7.

shear-dominated regime. However, we now consider the possibility of turbulent kinetic BLs even in pure RB flow which corresponds to the so-called 'ultimate' regime in RB flow (Kraichnan 1962; Grossmann & Lohse 2011; Roche 2020; Lohse & Shishkina 2023). While the existence of logarithmic temperature profiles has already been observed at high *Ra* (Grossmann & Lohse 2012; Ahlers *et al.* 2012; Ahlers, Bodenschatz & He 2014), it is yet to be seen if logarithmic behaviour given by

$$u_R^+(z^+) = \frac{1}{k}\log(z^+) + B, \tag{3.8}$$

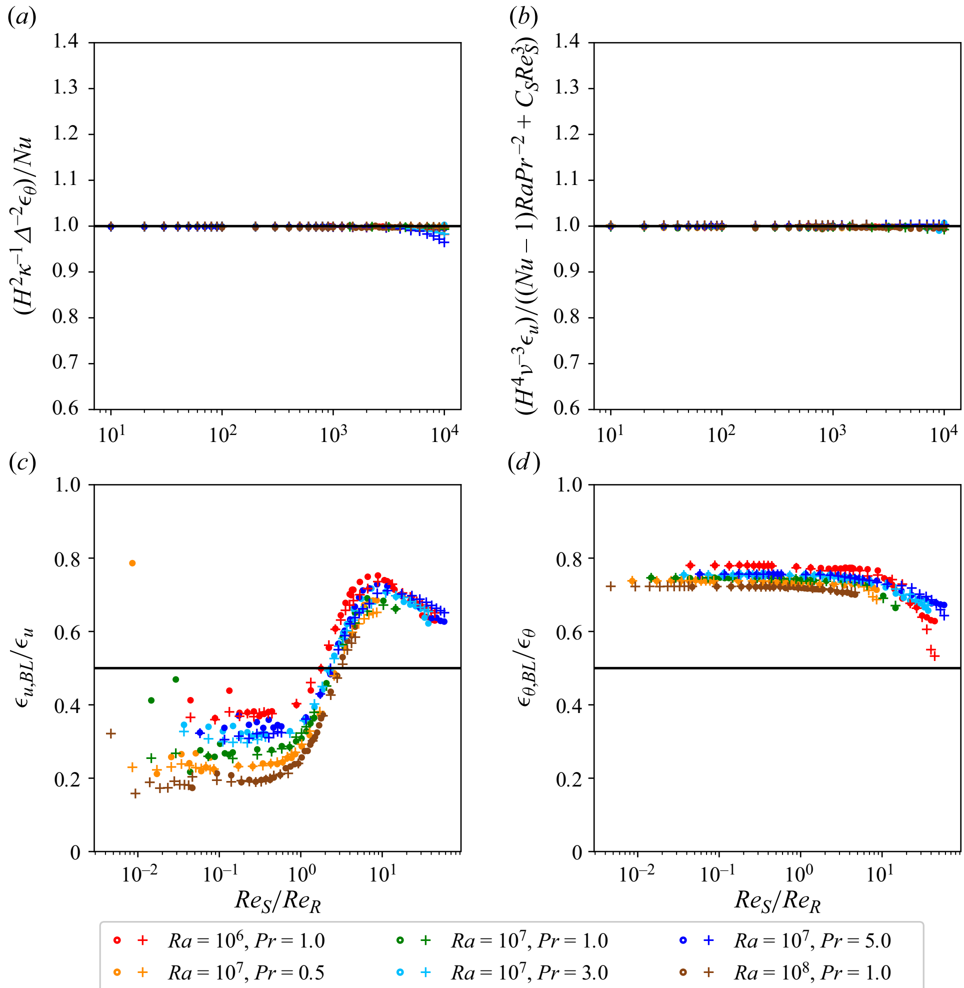

Figure 8. (*a*) Ratio $(H^2\epsilon_\theta\kappa^{-1}\Delta^2)/Nu$ showing good agreement with (2.1) indicated using the solid black line, and (*b*) ratio $(H^4\epsilon_u/\nu^3)/((Nu-1)RaPr^{-2}+C_SRe_S^3)$ plotted against Re_S showing good agreement with (2.2) of the manuscript shown using the solid black line. (*c*) Boundary layer contribution to the global kinetic dissipation rate $\epsilon_{u,BL}$ and (*d*) the BL contribution to the global thermal dissipation rate $\epsilon_{\theta,BL}$. The circle markers are for the CRB system, while plus markers are for the PRB system. This figure is also available at https://www.cambridge.org/S0022112024008723/JFM-Notebooks/files/figure8.

with

$$u_R^+(z^+) = u_R(z)/u_\tau, \quad z^+ = \frac{zu_\tau}{2\nu}, \quad u_R(z) \equiv \sqrt{\left\langle u_x^2 + u_y^2 \right\rangle_{A,t}}, \quad u_\tau = \sqrt{\nu\,\langle \partial_z u_R \rangle_{W,t}}, \tag{3.9a–d}$$

can be observed in the velocity profiles.

At the highest thermal forcing studied in this work with $Ra = 10^{12}$, we start to also observe some hints of what could possibly be the onset of a log layer (see figure 9*a*), although it cannot be conclusively confirmed with the currently available data. Assuming that such a log layer could exist, an estimate of the modified von Kármán constant k is obtained from the inflection point of the diagnostic function plotted in figure 9(*b*), giving

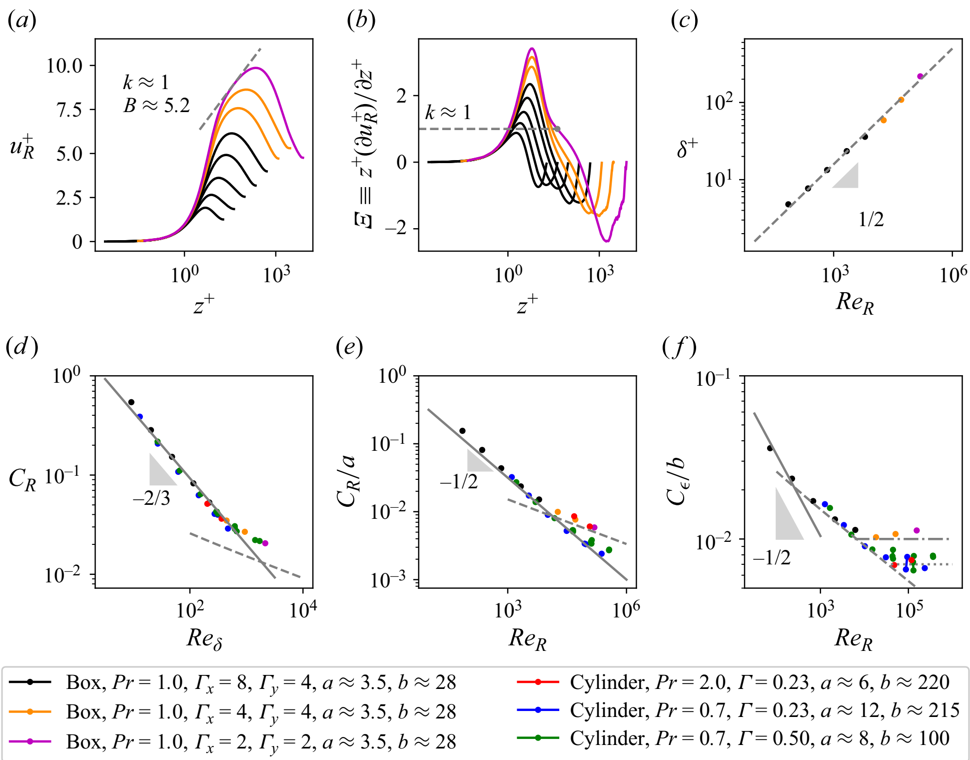

Figure 9. (*a*) Value of u_R^+ plotted against z^+, showing the onset of a log layer with the grey dashed line. The velocity profile for $Ra = 10^{12}$, $Pr = 1.0$ is indicated in magenta. (*b*) Diagnostic function plotted against z^+ with the inflection point and the corresponding von Kármán constant indicated. (*c*) Value of δ^+ plotted against Re_R shows good agreement with $\delta^+ = (1/2)Re_R^{1/2}$, indicated with the dashed grey line. (*d*) Value of C_R plotted against Re_δ showing a collapse without any prefactors. The solid grey line indicates $C_R \sim 4Re_\delta^{-2/3}$ and the dashed grey line indicates the modified Prandtl (1932) friction law given by (3.10*a*,*b*). (*e*) Value of C_R/a plotted against Re_R, showing the Prandtl–Blasius scaling (2.18) at low Re_R with the solid grey line and modified Prandtl (1932) friction law given by (3.10*a*,*b*) at high Re_R with the dashed grey line. (*f*) Value of C_ϵ/b given by (3.11*b*) plotted against Re_R. The solid grey line indicates $C_\epsilon \sim Re_R^{-1/2}$ for the regime with $\epsilon_u \sim \epsilon_{u,BL}$, the dashed grey line indicates the modified Prandtl (1932) friction law (3.10*a*,*b*). At higher Re_R, $\epsilon_u \sim \epsilon_{u,bulk}$, leading to C_ϵ becoming independent of Re_R, as indicated with the dash-dotted and dotted grey lines. This figure is also available at https://www.cambridge.org/S0022112024008723/JFM-Notebooks/files/figure9.

$k \approx 1$. Correspondingly, the intercept $B \approx 5.2$ is found by fitting the data, as shown in figure 9(*a*).

In the presence of such a logarithmic layer, we can now hypothesise about a relation for C_R which is analogous to relation (3.4) for C_S and (2.22) for C_T by stating that in the limit of highly turbulent BL, $u_R^+ = U_R$ at $z^+ = \delta^+$, where δ is the wall-normal distance to the peak velocity shown in figure 4. This gives us

$$\sqrt{\frac{2}{C_R}} = \frac{1}{k}\ln\left(Re_\delta\sqrt{\frac{C_R}{8}}\right) + B, \qquad Re_\delta = U_R\delta/\nu. \tag{3.10a,b}$$

If applicable to high Ra RB flow, the general form of this equation could suggest universality in the behaviour of wall-bounded flows even though the values of k and B might be different from those observed for pipe or channel flows. By plotting δ^+ against

Re_R, we find a very good fit with the scaling $\delta^+ \sim Re_R^{1/2}$, as shown in figure 9(*c*). At present, we can only provide this scaling empirically because more data at extremely high Ra are needed to understand the dynamics of the turbulent BL which is difficult due to the high computational expense of such numerical simulations. Plotting C_R against Re_δ in 9(*d*), we find a nice collapse of the data for different aspect ratios and geometries. At low Re_R, C_R seems to scale as $Re_\delta^{-2/3}$, which can be obtained from the empirical scaling $\delta^+ \sim Re_R^{1/2}$ shown in figure 9(*c*) and the assumption of a Prandtl–Blasius-type scaling of $C_R \sim Re_R^{-1/2}$. At high Re_R, we see good qualitative agreement between the data and the modified Prandtl (1932) friction law given by (3.10*a,b*).

We can further investigate the behaviour of C_R by computing

$$C_R \equiv aRe_R^{-1/2}, \tag{3.11a}$$

$$C_\epsilon \equiv b(Nu-1)RaPr^{-2}Re_R^{-3}, \quad \begin{cases} C_\epsilon \sim C_R & \text{if } \epsilon_u \sim \epsilon_{u,BL} \\ C_\epsilon = \text{const.} & \text{if } \epsilon_u \sim \epsilon_{u,bulk}, \end{cases} \tag{3.11b}$$

where a and b are prefactors that are obtained by fitting the data from figures 9(*e*) and 9(*f*), accounting for the effects of aspect ratio and geometry. Note that, when the kinetic dissipation of the RB system is dominated by the contribution from the BL, $C_\epsilon \sim C_R$ in (3.11*b*). The data points at lower Re_R in figure 9(*e*) are observed to follow (2.18), which is consistent with the Prandtl–Blasius scaling. For higher Re_R, corresponding to $Ra > 10^{10}$, C_R shows better agreement with the Prandtl (1932) friction law given by (3.10*a,b*). Figure 9(*f*) shows a very similar behaviour to figure 9(*e*) but, in addition, we observe that C_ϵ becomes independent of Re_R at very high values of Re_R. Although this does not reflect the true dependence of C_R on Re_R, this apparent dependence is expected because the kinetic dissipation of the RB system undergoes a transition from being dominated by the BL to being dominated by the bulk (Lohse 1994). It should also be noted that this transition occurs at higher Re_R for the more confined cylindrical RB simulations because more kinetic driving is required to overcome the viscous dissipation in the additional BLs on the side walls that are not present in the periodic box RB simulations (Ahlers *et al.* 2022).

4. Conclusions

In summary, we have developed a framework by extending the GL-theory for RB turbulence to sheared RB turbulence. As in the case of RB flow, we observe that there are no pure scaling exponents for the Nusselt number Nu and the friction coefficient C_S. This also holds for high thermal or shear driving where the BLs no longer obey scaling relations associated with the Prandtl–Blasius (Prandtl 1904; Blasius 1908) BL theory but start to become more turbulent. In such cases, we observe that the relation for $C_S(Re_S)$ is well described by the friction law of Prandtl (1932). In addition, we find that a modified version of the Prandtl's (1932) friction law for the large-scale circulation rolls $C_L(Re_L)$ analogous to $C_S(Re_S)$ agrees well with the DNS data, suggesting some sort of universality in the relation between the shear stress and the flow velocity that generates that shear.

It is also interesting to note that the relations are identical for CRB or PRB systems once the appropriate velocity scale is chosen as a control parameter. This suggests that the flow physics is not strongly affected by the geometry of the system or by the way in which shear forcing is applied. The flow characteristics of these systems are essentially determined by the ratio of shear driving to thermal driving, given by Re_S/Re_R. Applying shear to the RB system causes increased coherence in the streamwise direction and leads to a re-orientation of the LSC rolls and causes them to align more in the spanwise direction, with the thermal plumes also transporting the momentum imparted by the shear forcing. In the buoyancy-dominated regime with $Re_S \simeq Re_R$, this may lead to enhanced streamwise mixing between hot and cold plumes at a time scale that is smaller than the time scale of heat diffusion at the wall. This leads to heat entrapment in the bulk and a reduction in Nu.

Taking into account the orientation of the LSC rolls and the bulk dominance of ϵ_u in the buoyancy-dominated regime, we show that the orientation of large-scale flow structures can also be predicted to a reasonable degree by the ratio Re_S/Re_R, and we provide scaling relations for the $Nu(Re_S/Re_R)$ and $C_S(Re_S/Re_R)$, which are shown to agree well with the numerical simulations for $10^6 \leq Ra \leq 10^8$, $0.5 \leq Pr \leq 5.0$ and $0 \leq Re_S \leq 10^4$. However, the evidence from the DNS is limited at the moment due to its high computational costs, thereby restricting the parameter range in which the proposed scaling laws can be validated. Simulations for very high or very low values of Pr as well as for high Ra or Re_S can be very demanding, and it remains to be seen if the assumptions made in this work and the extended theory hold well in other control parameter ranges.

Supplementary material. Computational Notebook files are available as supplementary material at https://doi.org/10.1017/jfm.2024.872 and online at https://www.cambridge.org/S0022112024008723/JFM-Notebooks.

Acknowledgements. The authors gratefully acknowledge R. Hartmann, A. Blass and M. De Paoli for fruitful discussions.

Funding. This work was financially supported by the ERC starting grant (2018) for the project 'UltimateRB' and the Twente Max-Planck Center. This work was carried out on the Dutch national e-infrastructure with the support of SURF Cooperative. We acknowledge PRACE for awarding us access to MareNostrum at Barcelona Supercomputing Center (BSC), Spain (Project 2020225335 and 2020235589). The authors gratefully acknowledge the Gauss Centre for Supercomputing e.V. (www.gauss-centre.eu) for funding this project by providing computing time on the GCS Supercomputer SuperMUC at Leibniz Supercomputing Centre (www.lrz.de).

Declaration of interests. The authors report no conflict of interest.

Author ORCIDs.
- Guru Sreevanshu Yerragolam https://orcid.org/0000-0002-8928-2029;
- Christopher J. Howland https://orcid.org/0000-0003-3686-9253;
- Richard J.A.M. Stevens https://orcid.org/0000-0001-6976-5704;
- Roberto Verzicco https://orcid.org/0000-0002-2690-9998;
- Olga Shishkina https://orcid.org/0000-0002-6773-6464;
- Detlef Lohse https://orcid.org/0000-0003-4138-2255.

Author contributions. The theoretical framework was developed by D.L., O.S., R.J.A.M.S., C.J.H. and G.S.Y. The code 'AFiD' for the DNS was developed by R.V. while the numerical simulations were performed by G.S.Y. All authors were involved in the preparation of the manuscript.

Appendix. Simulation parameters

In table 3 we provide the physical and numerical input parameters used for the new sheared RB simulations conducted for this study. In addition to the new simulations, data for large aspect ratio simulations with $\Gamma_x = 48$ and $\Gamma_y = 24$ are taken from Yerragolam *et al.* (2022*b*), and data for high Ra cylindrical simulations are taken from Hartmann *et al.* (2023).

System	Γ_x	Γ_y	N_x	N_y	N_z	x^+	y^+	z_w^+	z_m^+	N_{BL}	Ra	Pr	Re_S	Nu_w	Nu_{ϵ_θ}	Nu_{ϵ_u}	C_S
RB	8	4	1024	512	192	—	—	—	—	41	10^5	1.0	0	4.38	4.38	4.38	—
RB	8	4	1536	768	256	—	—	—	—	40	10^6	1.0	0	8.31	8.31	8.32	—
RB	8	4	1536	768	256	—	—	—	—	29	10^7	0.5	0	15.32	15.33	15.32	—
RB	8	4	1536	768	256	—	—	—	—	28	10^7	1.0	0	15.75	14.47	15.73	—
RB	8	4	2048	1024	384	—	—	—	—	42	10^7	3.0	0	16.05	16.04	16.02	—
RB	8	4	2048	1024	384	—	—	—	—	42	10^7	5.0	0	16.14	16.14	16.19	—
RB	8	4	2048	1024	384	—	—	—	—	29	10^8	1.0	0	30.68	30.68	30.71	—
RB	8	4	3072	1536	512	—	—	—	—	28	10^9	1.0	0	61.83	61.86	61.98	—
RB	4	4	2048	2048	768	—	—	—	—	28	10^{10}	1.0	0	129.78	129.80	129.80	—
RB	4	4	3072	3072	1024	—	—	—	—	24	10^{11}	1.0	0	287.97	288.02	287.26	—
RB	2	2	2048	2048	1536	—	—	—	—	23	10^{12}	1.0	0	709.21	709.50	732.83	—
CRB	8	4	1536	768	256	0.05	0.05	0.00	0.05	40	10^6	1.0	10	8.26	8.27	8.27	1.56
CRB	8	4	1536	768	256	0.08	0.08	0.00	0.09	40	10^6	1.0	20	8.29	8.29	8.29	1.09
CRB	8	4	1536	768	256	0.07	0.07	0.00	0.09	40	10^6	1.0	30	8.26	8.26	8.25	0.459
CRB	8	4	1536	768	256	0.11	0.11	0.00	0.12	40	10^6	1.0	40	8.28	8.27	8.26	0.511
CRB	8	4	1536	768	256	0.12	0.12	0.00	0.14	40	10^6	1.0	50	8.26	8.26	8.25	0.399
CRB	8	4	1536	768	256	0.13	0.13	0.00	0.15	40	10^6	1.0	60	8.29	8.29	8.29	0.327
CRB	8	4	1536	768	256	0.14	0.14	0.00	0.17	40	10^6	1.0	70	8.25	8.24	8.24	0.3
CRB	8	4	1536	768	256	0.15	0.15	0.00	0.17	40	10^6	1.0	80	8.21	8.21	8.22	0.251
CRB	8	4	1536	768	256	0.16	0.16	0.00	0.18	40	10^6	1.0	90	8.19	8.19	8.18	0.224
CRB	8	4	1536	768	256	0.17	0.17	0.00	0.19	40	10^6	1.0	100	8.18	8.18	8.19	0.203
CRB	8	4	1536	768	256	0.23	0.23	0.00	0.28	41	10^6	1.0	200	7.84	7.84	7.85	0.102
CRB	8	4	1536	768	256	0.29	0.29	0.00	0.34	42	10^6	1.0	300	7.47	7.47	7.47	0.0676
CRB	8	4	1536	768	256	0.34	0.34	0.00	0.40	43	10^6	1.0	400	6.97	6.97	6.95	0.0546
CRB	8	4	1536	768	256	0.39	0.39	0.01	0.45	44	10^6	1.0	500	6.66	6.67	6.66	0.0442
CRB	8	4	1536	768	256	0.43	0.43	0.01	0.51	45	10^6	1.0	600	6.46	6.46	6.45	0.038
CRB	8	4	1536	768	256	0.47	0.47	0.01	0.55	46	10^6	1.0	700	6.35	6.35	6.35	0.0332
CRB	8	4	1536	768	256	0.51	0.51	0.01	0.60	46	10^6	1.0	800	6.31	6.31	6.33	0.0296
CRB	8	4	1536	768	256	0.54	0.54	0.01	0.64	46	10^6	1.0	900	6.27	6.28	6.26	0.0268
CRB	8	4	1536	768	256	0.55	0.55	0.01	0.64	46	10^6	1.0	920	6.25	6.25	6.26	0.0261
CRB	8	4	1536	768	256	0.55	0.55	0.01	0.65	46	10^6	1.0	940	6.27	6.27	6.27	0.0255

Table 3. For caption see next page.

System	Γ_x	Γ_y	N_x	N_y	N_z	x^+	y^+	z_w^+	z_m^+	N_{BL}	Ra	Pr	Re_S	Nu_w	Nu_{ϵ_θ}	Nu_{ϵ_u}	C_S
CRB	8	4	1536	768	256	0.56	0.56	0.01	0.66	46	10^6	1.0	960	6.24	6.24	6.22	0.0252
CRB	8	4	1536	768	256	0.57	0.57	0.01	0.66	46	10^6	1.0	980	6.20	6.19	6.21	0.0245
CRB	8	4	1536	768	256	0.57	0.57	0.01	0.67	46	10^6	1.0	1000	6.21	6.21	6.21	0.0241
CRB	8	4	1536	768	256	0.63	0.63	0.01	0.74	46	10^6	1.0	1200	6.19	6.19	6.18	0.0203
CRB	8	4	1536	768	256	0.71	0.71	0.01	0.83	46	10^6	1.0	1500	6.19	6.19	6.19	0.0164
CRB	8	4	1536	768	256	0.82	0.82	0.01	0.97	46	10^6	1.0	2000	6.26	6.26	6.25	0.0125
CRB	8	4	1536	768	256	0.91	0.91	0.01	1.06	46	10^6	1.0	2400	6.29	6.29	6.30	0.0105
CRB	8	4	1536	768	256	0.95	0.95	0.01	1.12	45	10^6	1.0	2600	6.39	6.38	6.38	0.00988
CRB	8	4	1536	768	256	1.01	1.01	0.01	1.18	44	10^6	1.0	2800	6.72	6.72	6.73	0.00957
CRB	8	4	1536	768	256	1.05	1.05	0.02	1.23	44	10^6	1.0	3000	6.74	6.73	6.67	0.00897
CRB	8	4	1536	768	256	1.10	1.10	0.02	1.29	44	10^6	1.0	3200	6.92	6.92	6.86	0.00867
CRB	8	4	1536	768	256	1.31	1.31	0.02	1.54	41	10^6	1.0	4000	7.83	7.83	7.82	0.0079
CRB	8	4	1536	768	256	1.58	1.58	0.02	1.86	38	10^6	1.0	5000	9.16	9.16	9.12	0.00738
CRB	8	4	1536	768	256	1.85	1.85	0.03	2.17	35	10^6	1.0	6000	10.45	10.46	10.45	0.00702
CRB	8	4	1536	768	256	2.08	2.08	0.03	2.44	33	10^6	1.0	7000	11.51	11.50	11.51	0.00652
CRB	8	4	1536	768	256	2.35	2.35	0.03	2.76	31	10^6	1.0	8000	12.87	12.86	12.86	0.00639
CRB	8	4	1536	768	256	2.59	2.59	0.04	3.04	30	10^6	1.0	9000	13.92	13.92	13.91	0.00613
CRB	8	4	1536	768	256	2.86	2.86	0.04	3.35	29	10^6	1.0	10 000	15.18	15.17	15.17	0.00602
CRB	8	4	1536	768	256	0.03	0.03	0.00	0.03	29	10^7	0.5	10	15.30	15.30	15.30	0.543
CRB	8	4	1536	768	256	0.13	0.13	0.00	0.15	29	10^7	0.5	20	15.29	15.29	15.29	3.05
CRB	8	4	1536	768	256	0.12	0.12	0.00	0.14	29	10^7	0.5	30	15.32	15.32	15.33	1.14
CRB	8	4	1536	768	256	0.13	0.13	0.00	0.16	29	10^7	0.5	40	15.26	15.26	15.26	0.829
CRB	8	4	1536	768	256	0.17	0.17	0.00	0.20	29	10^7	0.5	50	15.26	15.27	15.26	0.843
CRB	8	4	1536	768	256	0.16	0.16	0.00	0.19	29	10^7	0.5	60	15.22	15.22	15.22	0.554
CRB	8	4	1536	768	256	0.22	0.22	0.00	0.26	29	10^7	0.5	70	15.31	15.31	15.33	0.746
CRB	8	4	1536	768	256	0.22	0.22	0.00	0.26	29	10^7	0.5	80	15.34	15.35	15.35	0.558
CRB	8	4	1536	768	256	0.21	0.21	0.00	0.25	29	10^7	0.5	90	15.26	15.26	15.24	0.398
CRB	8	4	1536	768	256	0.25	0.25	0.00	0.30	29	10^7	0.5	100	15.35	15.36	15.36	0.477
CRB	8	4	1536	768	256	0.35	0.35	0.01	0.41	29	10^7	0.5	200	15.31	15.31	15.31	0.227
CRB	8	4	1536	768	256	0.44	0.44	0.01	0.52	29	10^7	0.5	300	15.24	15.23	15.23	0.16
CRB	8	4	1536	768	256	0.49	0.49	0.01	0.58	29	10^7	0.5	400	15.21	15.21	15.21	0.112

Table 3. For caption see next page.

System	Γ_x	Γ_y	N_x	N_y	N_z	x^+	y^+	z_w^+	z_m^+	N_{BL}	Ra	Pr	Re_S	Nu_w	Nu_{ϵ_θ}	Nu_{ϵ_u}	C_S
CRB	8	4	1536	768	256	0.56	0.56	0.01	0.65	29	10^7	0.5	500	15.10	15.11	15.09	0.0918
CRB	8	4	1536	768	256	0.62	0.62	0.01	0.73	29	10^7	0.5	600	15.06	15.06	15.08	0.0786
CRB	8	4	1536	768	256	0.68	0.68	0.01	0.79	29	10^7	0.5	700	14.89	14.90	14.89	0.0688
CRB	8	4	1536	768	256	0.73	0.73	0.01	0.85	29	10^7	0.5	800	14.74	14.75	14.74	0.061
CRB	8	4	1536	768	256	0.78	0.78	0.01	0.91	29	10^7	0.5	900	14.58	14.58	14.57	0.055
CRB	8	4	1536	768	256	0.82	0.82	0.01	0.96	30	10^7	0.5	1000	14.48	14.47	14.47	0.049
CRB	8	4	1536	768	256	0.89	0.89	0.01	1.05	30	10^7	0.5	1200	14.22	14.22	14.20	0.041
CRB	8	4	1536	768	256	1.03	1.03	0.01	1.21	31	10^7	0.5	1500	13.64	13.65	13.63	0.035
CRB	8	4	1536	768	256	1.22	1.22	0.02	1.43	31	10^7	0.5	2000	12.92	12.92	12.92	0.0272
CRB	8	4	1536	768	256	1.50	1.50	0.02	1.77	33	10^7	0.5	3000	12.04	12.05	12.04	0.0185
CRB	8	4	1536	768	256	1.75	1.75	0.03	2.06	33	10^7	0.5	4000	11.64	11.64	11.65	0.0141
CRB	8	4	1536	768	256	1.99	1.99	0.03	2.34	33	10^7	0.5	5000	11.43	11.44	11.43	0.0117
CRB	8	4	1536	768	256	2.20	2.20	0.03	2.58	33	10^7	0.5	6000	11.48	11.48	11.47	0.00994
CRB	8	4	1536	768	256	2.41	2.41	0.03	2.83	33	10^7	0.5	7000	11.66	11.67	11.67	0.00873
CRB	8	4	1536	768	256	2.61	2.61	0.04	3.07	33	10^7	0.5	8000	11.92	11.92	11.91	0.00787
CRB	8	4	1536	768	256	2.83	2.83	0.04	3.32	32	10^7	0.5	9000	12.32	12.32	12.32	0.00729
CRB	8	4	1536	768	256	3.06	3.06	0.04	3.59	32	10^7	0.5	10 000	12.82	12.83	12.82	0.00689
CRB	8	4	1536	768	256	0.04	0.04	0.00	0.05	28	10^7	1.0	10	15.73	15.73	15.73	1.42
CRB	8	4	1536	768	256	0.06	0.06	0.00	0.06	28	10^7	1.0	20	15.77	15.77	15.78	0.56
CRB	8	4	1536	768	256	0.16	0.16	0.00	0.18	28	10^7	1.0	30	15.77	15.77	15.78	1.97
CRB	8	4	1536	768	256	0.14	0.14	0.00	0.16	28	10^7	1.0	40	15.66	15.66	15.69	0.853
CRB	8	4	1536	768	256	0.16	0.16	0.00	0.19	28	10^7	1.0	50	15.67	15.67	15.66	0.77
CRB	8	4	1536	768	256	0.18	0.18	0.00	0.21	28	10^7	1.0	60	15.68	15.69	15.69	0.679
CRB	8	4	1536	768	256	0.16	0.16	0.00	0.19	28	10^7	1.0	70	15.79	15.79	15.82	0.391
CRB	8	4	1536	768	256	0.19	0.19	0.00	0.23	28	10^7	1.0	80	15.74	15.74	15.70	0.425
CRB	8	4	1536	768	256	0.21	0.21	0.00	0.24	28	10^7	1.0	90	15.76	15.76	15.74	0.391
CRB	8	4	1536	768	256	0.21	0.21	0.00	0.25	28	10^7	1.0	100	15.76	15.76	15.76	0.338
CRB	8	4	1536	768	256	0.30	0.30	0.00	0.35	28	10^7	1.0	200	15.64	15.65	15.66	0.168
CRB	8	4	1536	768	256	0.37	0.37	0.01	0.43	28	10^7	1.0	300	15.58	15.57	15.60	0.112
CRB	8	4	1536	768	256	0.44	0.44	0.01	0.51	29	10^7	1.0	400	15.45	15.44	15.47	0.0878
CRB	8	4	1536	768	256	0.50	0.50	0.01	0.59	29	10^7	1.0	500	15.08	15.07	15.08	0.0745

Table 3. For caption see next page.

System	Γ_x	Γ_y	N_x	N_y	N_z	x^+	y^+	z_w^+	z_m^+	N_{BL}	Ra	Pr	Re_S	Nu_w	Nu_{ϵ_θ}	Nu_{ϵ_u}	C_S
CRB	8	4	1536	768	256	0.55	0.55	0.01	0.64	29	10^7	1.0	600	14.93	14.91	14.93	0.0615
CRB	8	4	1536	768	256	0.61	0.61	0.01	0.71	29	10^7	1.0	700	14.62	14.62	14.62	0.0552
CRB	8	4	1536	768	256	0.66	0.66	0.01	0.77	30	10^7	1.0	800	14.27	14.27	14.28	0.0497
CRB	8	4	1536	768	256	0.70	0.70	0.01	0.82	30	10^7	1.0	900	14.02	14.03	14.03	0.0443
CRB	8	4	1536	768	256	0.75	0.75	0.01	0.88	30	10^7	1.0	1000	13.78	13.77	13.78	0.0413
CRB	8	4	1536	768	256	0.91	0.91	0.01	1.07	31	10^7	1.0	1414	12.93	12.93	12.93	0.0306
CRB	8	4	1536	768	256	1.17	1.17	0.02	1.37	33	10^7	1.0	2236	11.97	11.98	11.96	0.0201
CRB	8	4	1536	768	256	1.39	1.39	0.02	1.64	33	10^7	1.0	3162	11.62	11.62	11.61	0.0143
CRB	8	4	1536	768	256	1.69	1.69	0.02	1.98	33	10^7	1.0	4472	11.77	11.77	11.76	0.0105
CRB	8	4	1536	768	256	2.30	2.30	0.03	2.69	30	10^7	1.0	7071	13.74	13.74	13.69	0.00777
CRB	8	4	1536	768	256	3.08	3.08	0.04	3.62	27	10^7	1.0	10 000	17.44	17.44	17.50	0.00701
CRB	8	4	1536	768	256	0.05	0.05	0.00	0.06	28	10^7	3.0	10	16.03	16.03	16.04	1.98
CRB	8	4	1536	768	256	0.07	0.07	0.00	0.09	28	10^7	3.0	20	16.07	16.07	16.07	1.03
CRB	8	4	1536	768	256	0.09	0.09	0.00	0.11	28	10^7	3.0	30	16.03	16.02	16.02	0.717
CRB	8	4	1536	768	256	0.10	0.10	0.00	0.12	28	10^7	3.0	40	16.06	16.06	16.06	0.503
CRB	8	4	1536	768	256	0.13	0.13	0.00	0.15	28	10^7	3.0	50	16.05	16.05	16.07	0.469
CRB	8	4	1536	768	256	0.13	0.13	0.00	0.16	28	10^7	3.0	60	16.07	16.06	16.07	0.367
CRB	8	4	1536	768	256	0.15	0.15	0.00	0.18	28	10^7	3.0	70	16.03	16.03	16.04	0.345
CRB	8	4	1536	768	256	0.16	0.16	0.00	0.19	28	10^7	3.0	80	16.00	16.00	16.01	0.296
CRB	8	4	1536	768	256	0.17	0.17	0.00	0.20	28	10^7	3.0	90	15.98	15.97	15.97	0.269
CRB	8	4	1536	768	256	0.18	0.18	0.00	0.21	28	10^7	3.0	100	15.95	15.95	15.97	0.237
CRB	8	4	1536	768	256	0.26	0.26	0.00	0.30	28	10^7	3.0	200	15.56	15.55	15.58	0.12
CRB	8	4	1536	768	256	0.31	0.31	0.00	0.37	29	10^7	3.0	300	15.04	15.04	15.04	0.0807
CRB	8	4	1536	768	256	0.37	0.37	0.01	0.43	30	10^7	3.0	400	14.47	14.47	14.47	0.0622
CRB	8	4	1536	768	256	0.43	0.43	0.01	0.51	30	10^7	3.0	500	13.85	13.85	13.85	0.0555
CRB	8	4	1536	768	256	0.49	0.49	0.01	0.57	31	10^7	3.0	600	13.41	13.41	13.42	0.0482
CRB	8	4	1536	768	256	0.53	0.53	0.01	0.62	31	10^7	3.0	700	13.09	13.09	13.09	0.0421
CRB	8	4	1536	768	256	0.57	0.57	0.01	0.67	31	10^7	3.0	800	12.84	12.84	12.85	0.0372
CRB	8	4	1536	768	256	0.60	0.60	0.01	0.71	32	10^7	3.0	900	12.62	12.62	12.63	0.0333
CRB	8	4	1536	768	256	0.64	0.64	0.01	0.75	32	10^7	3.0	1000	12.47	12.47	12.47	0.0301
CRB	8	4	1536	768	256	0.70	0.70	0.01	0.83	32	10^7	3.0	1200	12.17	12.16	12.13	0.0254

Table 3. For caption see next page.

System	Γ_x	Γ_y	N_x	N_y	N_z	x^+	y^+	z_w^+	z_m^+	N_{BL}	Ra	Pr	Re_S	Nu_w	Nu_{ϵ_θ}	Nu_{ϵ_u}	C_S
CRB	8	4	1536	768	256	0.79	0.79	0.01	0.92	33	10^7	3.0	1500	12.05	12.06	12.06	0.0204
CRB	8	4	1536	768	256	0.95	0.95	0.01	1.12	32	10^7	3.0	2000	12.81	12.81	12.80	0.0167
CRB	8	4	1536	768	256	1.14	1.14	0.02	1.34	32	10^7	3.0	3000	12.59	12.59	12.58	0.0106
CRB	8	4	1536	768	256	1.38	1.38	0.02	1.62	30	10^7	3.0	4000	14.00	14.00	14.04	0.00878
CRB	8	4	1536	768	256	1.64	1.64	0.02	1.92	28	10^7	3.0	5000	15.98	15.97	15.97	0.00788
CRB	8	4	1536	768	256	1.90	1.90	0.03	2.23	26	10^7	3.0	6000	18.15	18.16	18.18	0.00739
CRB	8	4	1536	768	256	2.16	2.16	0.03	2.54	25	10^7	3.0	7000	20.34	20.31	20.29	0.00705
CRB	8	4	1536	768	256	2.44	2.44	0.03	2.86	23	10^7	3.0	8000	22.73	22.74	22.71	0.00683
CRB	8	4	1536	768	256	2.63	2.63	0.04	3.08	23	10^7	3.0	9000	24.18	24.11	24.00	0.00629
CRB	8	4	1536	768	256	2.87	2.87	0.04	3.37	22	10^7	3.0	10 000	26.23	26.36	26.93	0.00609
CRB	8	4	2048	1024	384	0.04	0.04	0.00	0.04	41	10^7	5.0	10	16.13	16.13	16.13	2.13
CRB	8	4	2048	1024	384	0.06	0.06	0.00	0.06	41	10^7	5.0	20	16.14	16.14	16.15	1.03
CRB	8	4	2048	1024	384	0.06	0.06	0.00	0.06	41	10^7	5.0	30	16.13	16.12	16.14	0.553
CRB	8	4	2048	1024	384	0.08	0.08	0.00	0.08	41	10^7	5.0	40	16.11	16.11	16.11	0.481
CRB	8	4	2048	1024	384	0.08	0.08	0.00	0.09	41	10^7	5.0	50	16.09	16.09	16.08	0.368
CRB	8	4	2048	1024	384	0.09	0.09	0.00	0.10	41	10^7	5.0	60	16.04	16.04	16.03	0.324
CRB	8	4	2048	1024	384	0.10	0.10	0.00	0.10	41	10^7	5.0	70	16.02	16.02	16.02	0.264
CRB	8	4	2048	1024	384	0.11	0.11	0.00	0.11	41	10^7	5.0	80	15.93	15.93	15.91	0.253
CRB	8	4	2048	1024	384	0.12	0.12	0.00	0.12	41	10^7	5.0	90	15.98	15.98	15.97	0.217
CRB	8	4	2048	1024	384	0.12	0.12	0.00	0.13	41	10^7	5.0	100	15.85	15.85	15.85	0.201
CRB	8	4	2048	1024	384	0.18	0.18	0.00	0.19	42	10^7	5.0	200	15.09	15.09	15.10	0.108
CRB	8	4	2048	1024	384	0.23	0.23	0.01	0.23	44	10^7	5.0	300	14.33	14.33	14.34	0.0751
CRB	8	4	2048	1024	384	0.26	0.26	0.01	0.27	45	10^7	5.0	400	13.78	13.78	13.78	0.0552
CRB	8	4	2048	1024	384	0.31	0.31	0.01	0.32	46	10^7	5.0	500	13.18	13.18	13.18	0.0492
CRB	8	4	2048	1024	384	0.34	0.34	0.01	0.35	46	10^7	5.0	600	12.91	12.91	13.00	0.0411
CRB	8	4	2048	1024	384	0.36	0.36	0.01	0.38	47	10^7	5.0	700	12.67	12.67	12.77	0.0354
CRB	8	4	2048	1024	384	0.40	0.40	0.01	0.42	46	10^7	5.0	800	12.84	12.84	12.87	0.0332
CRB	8	4	2048	1024	384	0.43	0.43	0.01	0.45	46	10^7	5.0	900	12.94	12.94	12.89	0.0303
CRB	8	4	2048	1024	384	0.46	0.46	0.01	0.48	46	10^7	5.0	1000	13.07	13.07	13.04	0.028
CRB	8	4	2048	1024	384	0.48	0.48	0.01	0.50	48	10^7	5.0	1200	12.20	12.20	12.21	0.0211
CRB	8	4	2048	1024	384	0.54	0.54	0.01	0.56	48	10^7	5.0	1500	12.19	12.19	12.19	0.017

Table 3. For caption see next page.

System	Γ_x	Γ_y	N_x	N_y	N_z	x^+	y^+	z_w^+	z_m^+	N_{BL}	Ra	Pr	Re_S	Nu_w	Nu_{ϵ_θ}	Nu_{ϵ_u}	C_S
CRB	8	4	2048	1024	384	0.62	0.62	0.02	0.64	47	10^7	5.0	2000	12.28	12.28	12.27	0.0128
CRB	8	4	2048	1024	384	0.80	0.80	0.02	0.83	44	10^7	5.0	3000	13.98	13.98	13.96	0.00942
CRB	8	4	2048	1024	384	1.00	1.00	0.03	1.03	40	10^7	5.0	4000	16.44	16.44	16.39	0.00818
CRB	8	4	2048	1024	384	1.20	1.20	0.03	1.24	37	10^7	5.0	5000	19.14	19.13	19.14	0.0075
CRB	8	4	2048	1024	384	1.39	1.39	0.03	1.43	35	10^7	5.0	6000	21.72	21.72	21.88	0.007
CRB	8	4	2048	1024	384	1.56	1.56	0.04	1.61	33	10^7	5.0	7000	24.23	24.24	24.31	0.0065
CRB	8	4	2048	1024	384	1.76	1.76	0.04	1.82	31	10^7	5.0	8000	27.10	27.08	27.10	0.00637
CRB	8	4	2048	1024	384	1.94	1.94	0.05	2.01	29	10^7	5.0	9000	29.63	29.60	29.53	0.0061
CRB	8	4	2048	1024	384	2.15	2.15	0.05	2.22	28	10^7	5.0	10 000	32.59	32.54	32.42	0.00603
CRB	8	4	2048	1024	384	0.26	0.26	0.01	0.27	29	10^8	1.0	100	30.85	30.86	30.85	0.893
CRB	8	4	2048	1024	384	0.29	0.29	0.01	0.30	29	10^8	1.0	200	30.68	30.68	30.78	0.281
CRB	8	4	2048	1024	384	0.36	0.36	0.01	0.37	29	10^8	1.0	300	30.80	30.80	30.84	0.188
CRB	8	4	2048	1024	384	0.47	0.47	0.01	0.49	29	10^8	1.0	400	30.81	30.80	30.87	0.183
CRB	8	4	2048	1024	384	0.51	0.51	0.01	0.53	29	10^8	1.0	500	30.79	30.79	30.81	0.138
CRB	8	4	2048	1024	384	0.58	0.58	0.01	0.60	29	10^8	1.0	600	30.72	30.73	30.74	0.124
CRB	8	4	2048	1024	384	0.63	0.63	0.02	0.65	29	10^8	1.0	700	30.69	30.70	30.64	0.105
CRB	8	4	2048	1024	384	0.66	0.66	0.02	0.68	29	10^8	1.0	800	30.66	30.65	30.71	0.0879
CRB	8	4	2048	1024	384	0.72	0.72	0.02	0.74	29	10^8	1.0	900	30.55	30.54	30.49	0.0836
CRB	8	4	2048	1024	384	0.75	0.75	0.02	0.78	29	10^8	1.0	1000	30.49	30.53	30.55	0.0743
CRB	8	4	2048	1024	384	0.80	0.80	0.02	0.83	29	10^8	1.0	1200	30.45	30.45	30.50	0.0587
CRB	8	4	2048	1024	384	0.92	0.92	0.02	0.95	29	10^8	1.0	1400	29.97	30.10	29.66	0.056
CRB	8	4	2048	1024	384	0.97	0.97	0.02	1.00	29	10^8	1.0	1600	29.80	29.80	29.77	0.0481
CRB	8	4	2048	1024	384	1.03	1.03	0.03	1.06	29	10^8	1.0	1800	29.54	29.53	29.52	0.0426
CRB	8	4	2048	1024	384	1.09	1.09	0.03	1.13	30	10^8	1.0	2000	29.19	29.20	29.20	0.0392
CRB	8	4	2048	1024	384	1.17	1.17	0.03	1.21	30	10^8	1.0	2200	28.73	28.74	28.67	0.0371
CRB	8	4	2048	1024	384	1.25	1.25	0.03	1.29	30	10^8	1.0	2400	28.46	28.57	27.48	0.0356
CRB	8	4	2048	1024	384	1.28	1.28	0.03	1.32	30	10^8	1.0	2600	28.16	28.16	28.11	0.0318
CRB	8	4	2048	1024	384	1.32	1.32	0.03	1.37	30	10^8	1.0	2800	28.07	28.07	28.07	0.0292
CRB	8	4	2048	1024	384	1.37	1.37	0.03	1.42	30	10^8	1.0	2900	27.82	27.83	27.87	0.0292
CRB	8	4	2048	1024	384	1.40	1.40	0.03	1.44	30	10^8	1.0	3000	27.68	27.68	27.67	0.0284
CRB	8	4	2048	1024	384	1.44	1.44	0.04	1.49	31	10^8	1.0	3200	27.40	27.42	27.48	0.0265

Table 3. For caption see next page.

System	Γ_x	Γ_y	N_x	N_y	N_z	x^+	y^+	z_w^+	z_m^+	N_{BL}	Ra	Pr	Re_S	Nu_w	Nu_{ϵ_θ}	Nu_{ϵ_u}	C_S
CRB	8	4	2048	1024	384	1.49	1.49	0.04	1.54	31	10^8	1.0	3400	27.16	27.16	27.02	0.0252
CRB	8	4	2048	1024	384	1.54	1.54	0.04	1.60	31	10^8	1.0	3600	26.99	27.00	27.01	0.0241
CRB	8	4	2048	1024	384	1.60	1.60	0.04	1.65	31	10^8	1.0	3800	26.80	26.80	26.74	0.0232
CRB	8	4	2048	1024	384	1.64	1.64	0.04	1.69	31	10^8	1.0	4000	26.60	26.63	26.58	0.022
CRB	8	4	2048	1024	384	1.85	1.85	0.05	1.91	32	10^8	1.0	5000	26.05	26.07	26.18	0.0179
CRB	8	4	2048	1024	384	2.05	2.05	0.05	2.12	32	10^8	1.0	6000	25.57	25.60	25.77	0.0153
CRB	8	4	2048	1024	384	2.24	2.24	0.06	2.32	32	10^8	1.0	7000	25.19	25.19	25.19	0.0134
CRB	8	4	2048	1024	384	2.44	2.44	0.06	2.52	32	10^8	1.0	8000	25.32	25.33	25.36	0.0121
CRB	8	4	2048	1024	384	2.60	2.60	0.07	2.69	32	10^8	1.0	9000	25.49	25.49	25.61	0.011
CRB	8	4	2048	1024	384	2.77	2.77	0.07	2.86	32	10^8	1.0	10 000	25.69	25.68	25.64	0.0101
PRB	8	4	1536	768	256	0.05	0.05	0.00	0.06	40	10^6	1.0	10	8.25	8.25	8.25	2.15
PRB	8	4	1536	768	256	0.08	0.08	0.00	0.09	40	10^6	1.0	20	8.31	8.31	8.31	1.15
PRB	8	4	1536	768	256	0.09	0.09	0.00	0.10	40	10^6	1.0	30	8.30	8.31	8.31	0.644
PRB	8	4	1536	768	256	0.11	0.11	0.00	0.13	40	10^6	1.0	40	8.28	8.28	8.28	0.524
PRB	8	4	1536	768	256	0.12	0.12	0.00	0.14	40	10^6	1.0	50	8.29	8.29	8.29	0.417
PRB	8	4	1536	768	256	0.13	0.13	0.00	0.16	40	10^6	1.0	60	8.26	8.26	8.26	0.358
PRB	8	4	1536	768	256	0.14	0.14	0.00	0.16	40	10^6	1.0	70	8.25	8.25	8.25	0.294
PRB	8	4	1536	768	256	0.15	0.15	0.00	0.18	40	10^6	1.0	80	8.19	8.19	8.19	0.259
PRB	8	4	1536	768	256	0.16	0.16	0.00	0.19	40	10^6	1.0	90	8.21	8.21	8.21	0.237
PRB	8	4	1536	768	256	0.17	0.17	0.00	0.20	40	10^6	1.0	100	8.17	8.16	8.17	0.216
PRB	8	4	1536	768	256	0.24	0.24	0.00	0.29	41	10^6	1.0	200	7.86	7.87	7.87	0.11
PRB	8	4	1536	768	256	0.30	0.30	0.00	0.35	42	10^6	1.0	300	7.37	7.36	7.36	0.0748
PRB	8	4	1536	768	256	0.36	0.36	0.01	0.42	43	10^6	1.0	400	7.04	7.04	7.04	0.0595
PRB	8	4	1536	768	256	0.41	0.41	0.01	0.48	44	10^6	1.0	500	6.74	6.74	6.74	0.0486
PRB	8	4	1536	768	256	0.45	0.45	0.01	0.53	45	10^6	1.0	600	6.56	6.56	6.56	0.0414
PRB	8	4	1536	768	256	0.49	0.49	0.01	0.57	45	10^6	1.0	700	6.43	6.43	6.44	0.0361
PRB	8	4	1536	768	256	0.53	0.53	0.01	0.62	45	10^6	1.0	800	6.39	6.38	6.38	0.0322
PRB	8	4	1536	768	256	0.57	0.57	0.01	0.67	46	10^6	1.0	900	6.35	6.35	6.35	0.0293
PRB	8	4	1536	768	256	0.60	0.60	0.01	0.70	46	10^6	1.0	1000	6.32	6.31	6.32	0.0266
PRB	8	4	1536	768	256	0.67	0.67	0.01	0.78	46	10^6	1.0	1200	6.31	6.30	6.30	0.0227
PRB	8	4	1536	768	256	0.80	0.80	0.01	0.94	43	10^6	1.0	1500	7.07	7.06	7.06	0.0211

Table 3. For caption see next page.

https://doi.org/10.1017/jfm.2024.872 Published online by Cambridge University Press

System	Γ_x	Γ_y	N_x	N_y	N_z	x^+	y^+	z_w^+	z_m^+	N_{BL}	Ra	Pr	Re_S	Nu_w	Nu_{ϵ_θ}	Nu_{ϵ_u}	C_S
PRB	8	4	1536	768	256	0.95	0.95	0.01	1.11	42	10^6	1.0	2000	7.34	7.32	7.33	0.0166
PRB	8	4	1536	768	256	1.13	1.13	0.02	1.32	44	10^6	1.0	3000	6.67	6.65	6.64	0.0104
PRB	8	4	1536	768	256	1.37	1.37	0.02	1.61	41	10^6	1.0	4000	7.59	7.57	7.55	0.00866
PRB	8	4	1536	768	256	1.68	1.68	0.02	1.97	39	10^6	1.0	5000	8.50	8.45	8.49	0.0083
PRB	8	4	1536	768	256	1.99	1.99	0.03	2.34	36	10^6	1.0	6000	10.05	9.99	10.08	0.00811
PRB	8	4	1536	768	256	2.28	2.28	0.03	2.68	34	10^6	1.0	7000	11.10	11.03	11.05	0.00785
PRB	8	4	1536	768	256	2.56	2.56	0.04	3.01	33	10^6	1.0	8000	11.64	11.54	11.60	0.00755
PRB	8	4	1536	768	256	2.83	2.83	0.04	3.32	33	10^6	1.0	9000	11.68	11.55	11.60	0.00731
PRB	8	4	1536	768	256	3.10	3.10	0.04	3.63	32	10^6	1.0	10 000	12.35	12.16	12.25	0.00707
PRB	8	4	1536	768	256	0.08	0.08	0.00	0.09	29	10^7	0.5	10	15.27	15.27	15.27	4.76
PRB	8	4	1536	768	256	0.12	0.12	0.00	0.14	29	10^7	0.5	20	15.29	15.30	15.30	2.57
PRB	8	4	1536	768	256	0.14	0.14	0.00	0.16	29	10^7	0.5	30	15.27	15.27	15.27	1.56
PRB	8	4	1536	768	256	0.15	0.15	0.00	0.18	29	10^7	0.5	40	15.24	15.25	15.25	1.07
PRB	8	4	1536	768	256	0.18	0.18	0.00	0.21	29	10^7	0.5	50	15.28	15.29	15.28	0.923
PRB	8	4	1536	768	256	0.20	0.20	0.00	0.23	29	10^7	0.5	60	15.26	15.26	15.27	0.82
PRB	8	4	1536	768	256	0.22	0.22	0.00	0.25	29	10^7	0.5	70	15.29	15.29	15.30	0.708
PRB	8	4	1536	768	256	0.23	0.23	0.00	0.27	29	10^7	0.5	80	15.23	15.23	15.23	0.607
PRB	8	4	1536	768	256	0.25	0.25	0.00	0.30	29	10^7	0.5	90	15.26	15.27	15.26	0.588
PRB	8	4	1536	768	256	0.26	0.26	0.00	0.31	29	10^7	0.5	100	15.30	15.31	15.30	0.511
PRB	8	4	1536	768	256	0.37	0.37	0.01	0.43	29	10^7	0.5	200	15.20	15.21	15.21	0.249
PRB	8	4	1536	768	256	0.44	0.44	0.01	0.52	29	10^7	0.5	300	15.21	15.21	15.22	0.159
PRB	8	4	1536	768	256	0.51	0.51	0.01	0.60	29	10^7	0.5	400	15.12	15.12	15.13	0.121
PRB	8	4	1536	768	256	0.57	0.57	0.01	0.67	29	10^7	0.5	500	15.09	15.10	15.09	0.0974
PRB	8	4	1536	768	256	0.62	0.62	0.01	0.73	29	10^7	0.5	600	15.02	15.02	15.03	0.0799
PRB	8	4	1536	768	256	0.68	0.68	0.01	0.80	29	10^7	0.5	700	14.91	14.91	14.92	0.0695
PRB	8	4	1536	768	256	0.72	0.72	0.01	0.85	29	10^7	0.5	800	14.82	14.81	14.81	0.06
PRB	8	4	1536	768	256	0.77	0.77	0.01	0.90	29	10^7	0.5	900	14.67	14.67	14.67	0.0537
PRB	8	4	1536	768	256	0.81	0.81	0.01	0.95	29	10^7	0.5	1000	14.59	14.60	14.60	0.0487
PRB	8	4	1536	768	256	0.90	0.90	0.01	1.06	30	10^7	0.5	1200	14.31	14.31	14.31	0.0415
PRB	8	4	1536	768	256	1.02	1.02	0.01	1.19	30	10^7	0.5	1500	13.85	13.85	13.86	0.0338
PRB	8	4	1536	768	256	1.19	1.19	0.02	1.40	31	10^7	0.5	2000	13.20	13.20	13.21	0.0262

Table 3. For caption see next page.

System	Γ_x	Γ_y	N_x	N_y	N_z	x^+	y^+	z_w^+	z_m^+	N_{BL}	Ra	Pr	Re_S	Nu_w	Nu_{ϵ_θ}	Nu_{ϵ_u}	C_S
PRB	8	4	1536	768	256	1.49	1.49	0.02	1.75	32	10^7	0.5	3000	12.24	12.23	12.24	0.0183
PRB	8	4	1536	768	256	1.74	1.74	0.03	2.05	33	10^7	0.5	4000	11.77	11.77	11.78	0.014
PRB	8	4	1536	768	256	1.96	1.96	0.03	2.30	33	10^7	0.5	5000	11.68	11.67	11.67	0.0114
PRB	8	4	1536	768	256	2.19	2.19	0.03	2.57	33	10^7	0.5	6000	11.69	11.68	11.68	0.00981
PRB	8	4	1536	768	256	2.42	2.42	0.03	2.84	33	10^7	0.5	7000	11.82	11.80	11.79	0.00878
PRB	8	4	1536	768	256	2.66	2.66	0.04	3.12	32	10^7	0.5	8000	12.10	12.08	12.09	0.00812
PRB	8	4	1536	768	256	2.93	2.93	0.04	3.44	32	10^7	0.5	9000	12.59	12.57	12.58	0.00781
PRB	8	4	1536	768	256	3.17	3.17	0.05	3.73	31	10^7	0.5	10 000	13.16	13.14	13.16	0.00743
PRB	8	4	1536	768	256	0.07	0.07	0.00	0.09	28	10^7	1.0	10	15.74	15.74	15.74	3.95
PRB	8	4	1536	768	256	0.10	0.10	0.00	0.11	28	10^7	1.0	20	15.73	15.74	15.74	1.73
PRB	8	4	1536	768	256	0.16	0.16	0.00	0.19	28	10^7	1.0	50	15.73	15.73	15.73	0.77
PRB	8	4	1536	768	256	0.23	0.23	0.00	0.27	28	10^7	1.0	100	15.74	15.75	15.75	0.395
PRB	8	4	1536	768	256	0.31	0.31	0.00	0.37	28	10^7	1.0	200	15.67	15.67	15.68	0.182
PRB	8	4	1536	768	256	0.39	0.39	0.01	0.45	29	10^7	1.0	300	15.54	15.55	15.55	0.123
PRB	8	4	1536	768	256	0.45	0.45	0.01	0.52	29	10^7	1.0	400	15.39	15.39	15.39	0.0913
PRB	8	4	1536	768	256	0.50	0.50	0.01	0.59	29	10^7	1.0	500	15.15	15.15	15.14	0.0746
PRB	8	4	1536	768	256	0.55	0.55	0.01	0.65	29	10^7	1.0	600	14.97	14.97	14.97	0.0625
PRB	8	4	1536	768	256	0.60	0.60	0.01	0.71	29	10^7	1.0	700	14.71	14.71	14.71	0.0548
PRB	8	4	1536	768	256	0.65	0.65	0.01	0.76	30	10^7	1.0	800	14.51	14.51	14.50	0.0488
PRB	8	4	1536	768	256	0.70	0.70	0.01	0.82	30	10^7	1.0	900	14.21	14.21	14.21	0.0442
PRB	8	4	1536	768	256	0.74	0.74	0.01	0.87	30	10^7	1.0	1000	13.99	13.99	14.00	0.0404
PRB	8	4	1536	768	256	0.90	0.90	0.01	1.06	31	10^7	1.0	1414	13.17	13.17	13.18	0.03
PRB	8	4	1536	768	256	1.16	1.16	0.02	1.36	32	10^7	1.0	2236	12.18	12.18	12.20	0.0197
PRB	8	4	1536	768	256	1.40	1.40	0.02	1.64	33	10^7	1.0	3162	11.86	11.85	11.87	0.0144
PRB	8	4	1536	768	256	1.71	1.71	0.02	2.01	33	10^7	1.0	4472	11.91	11.90	11.91	0.0108
PRB	8	4	1536	768	256	2.36	2.36	0.03	2.77	31	10^7	1.0	7071	13.29	13.25	13.30	0.0082
PRB	8	4	1536	768	256	3.16	3.16	0.05	3.71	27	10^7	1.0	10 000	17.11	17.02	17.04	0.00735
PRB	8	4	1536	768	256	0.05	0.05	0.00	0.06	28	10^7	3.0	10	16.11	16.11	16.12	2.14
PRB	8	4	1536	768	256	0.08	0.08	0.00	0.10	28	10^7	3.0	20	16.12	16.12	16.13	1.23
PRB	8	4	1536	768	256	0.10	0.10	0.00	0.12	28	10^7	3.0	30	16.12	16.11	16.12	0.829
PRB	8	4	1536	768	256	0.12	0.12	0.00	0.14	28	10^7	3.0	40	16.10	16.10	16.11	0.636

Table 3. For caption see next page.

System	Γ_x	Γ_y	N_x	N_y	N_z	x^+	y^+	z_w^+	z_m^+	N_{BL}	Ra	Pr	Re_S	Nu_w	Nu_{ϵ_θ}	Nu_{ϵ_u}	C_S
PRB	8	4	1536	768	256	0.13	0.13	0.00	0.15	28	10^7	3.0	50	16.05	16.05	16.06	0.488
PRB	8	4	1536	768	256	0.15	0.15	0.00	0.17	28	10^7	3.0	60	16.02	16.02	16.02	0.452
PRB	8	4	1536	768	256	0.15	0.15	0.00	0.18	28	10^7	3.0	70	16.05	16.05	16.05	0.347
PRB	8	4	1536	768	256	0.16	0.16	0.00	0.19	28	10^7	3.0	80	16.03	16.03	16.04	0.308
PRB	8	4	1536	768	256	0.17	0.17	0.00	0.20	28	10^7	3.0	90	16.00	16.00	16.01	0.275
PRB	8	4	1536	768	256	0.18	0.18	0.00	0.22	28	10^7	3.0	100	15.98	15.98	15.99	0.25
PRB	8	4	1536	768	256	0.26	0.26	0.00	0.31	28	10^7	3.0	200	15.55	15.55	15.56	0.126
PRB	8	4	1536	768	256	0.33	0.33	0.00	0.39	29	10^7	3.0	300	15.02	15.01	15.02	0.0897
PRB	8	4	1536	768	256	0.39	0.39	0.01	0.46	30	10^7	3.0	400	14.43	14.43	14.44	0.0705
PRB	8	4	1536	768	256	0.45	0.45	0.01	0.52	30	10^7	3.0	500	13.97	13.97	13.98	0.0585
PRB	8	4	1536	768	256	0.49	0.49	0.01	0.58	31	10^7	3.0	600	13.61	13.60	13.62	0.0497
PRB	8	4	1536	768	256	0.54	0.54	0.01	0.63	31	10^7	3.0	700	13.28	13.28	13.28	0.0436
PRB	8	4	1536	768	256	0.58	0.58	0.01	0.68	31	10^7	3.0	800	13.01	13.01	13.02	0.0384
PRB	8	4	1536	768	256	0.62	0.62	0.01	0.72	32	10^7	3.0	900	12.78	12.78	12.80	0.0345
PRB	8	4	1536	768	256	0.65	0.65	0.01	0.76	32	10^7	3.0	1000	12.65	12.64	12.65	0.0313
PRB	8	4	1536	768	256	0.72	0.72	0.01	0.85	32	10^7	3.0	1200	12.39	12.39	12.42	0.0266
PRB	8	4	1536	768	256	0.81	0.81	0.01	0.95	32	10^7	3.0	1500	12.26	12.25	12.27	0.0217
PRB	8	4	1536	768	256	0.95	0.95	0.01	1.12	32	10^7	3.0	2000	12.20	12.19	12.20	0.0167
PRB	8	4	1536	768	256	1.20	1.20	0.02	1.41	33	10^7	3.0	3000	12.09	12.08	12.08	0.0119
PRB	8	4	1536	768	256	1.44	1.44	0.02	1.69	31	10^7	3.0	4000	13.18	13.14	13.27	0.00954
PRB	8	4	1536	768	256	1.71	1.71	0.02	2.01	29	10^7	3.0	5000	14.92	14.85	14.90	0.00865
PRB	8	4	1536	768	256	1.99	1.99	0.03	2.33	27	10^7	3.0	6000	17.68	17.57	17.60	0.00808
PRB	8	4	1536	768	256	2.30	2.30	0.03	2.69	25	10^7	3.0	7000	20.20	20.02	20.23	0.00793
PRB	8	4	1536	768	256	2.58	2.58	0.04	3.03	23	10^7	3.0	8000	22.88	22.66	22.89	0.00768
PRB	8	4	1536	768	256	2.86	2.86	0.04	3.35	22	10^7	3.0	9000	25.00	24.70	25.00	0.00743
PRB	8	4	1536	768	256	3.13	3.13	0.04	3.67	21	10^7	3.0	10 000	26.99	26.59	26.96	0.0072
PRB	8	4	1536	768	256	0.05	0.05	0.00	0.06	28	10^7	5.0	10	16.20	16.19	16.20	2.16
PRB	8	4	1536	768	256	0.08	0.08	0.00	0.09	28	10^7	5.0	20	16.13	16.12	16.13	1.2
PRB	8	4	1536	768	256	0.10	0.10	0.00	0.11	28	10^7	5.0	30	16.11	16.11	16.11	0.778
PRB	8	4	1536	768	256	0.11	0.11	0.00	0.13	28	10^7	5.0	40	16.10	16.10	16.10	0.593
PRB	8	4	1536	768	256	0.12	0.12	0.00	0.14	28	10^7	5.0	50	16.10	16.10	16.11	0.42

Table 3. For caption see next page.

System	Γ_x	Γ_y	N_x	N_y	N_z	x^+	y^+	z_w^+	z_m^+	N_{BL}	Ra	Pr	Re_S	Nu_w	Nu_{ϵ_θ}	Nu_{ϵ_u}	C_S
PRB	8	4	1536	768	256	0.13	0.13	0.00	0.16	28	10^7	5.0	60	16.08	16.08	16.08	0.358
PRB	8	4	1536	768	256	0.15	0.15	0.00	0.18	28	10^7	5.0	70	16.01	16.01	16.02	0.341
PRB	8	4	1536	768	256	0.15	0.15	0.00	0.18	28	10^7	5.0	80	16.03	16.02	16.03	0.268
PRB	8	4	1536	768	256	0.16	0.16	0.00	0.19	28	10^7	5.0	90	15.94	15.94	15.95	0.239
PRB	8	4	1536	768	256	0.17	0.17	0.00	0.20	28	10^7	5.0	100	15.91	15.91	15.92	0.218
PRB	8	4	1536	768	256	0.25	0.25	0.00	0.30	29	10^7	5.0	200	15.18	15.17	15.18	0.118
PRB	8	4	1536	768	256	0.32	0.32	0.00	0.38	30	10^7	5.0	300	14.37	14.37	14.38	0.0838
PRB	8	4	1536	768	256	0.37	0.37	0.01	0.44	30	10^7	5.0	400	13.78	13.78	13.79	0.0648
PRB	8	4	1536	768	256	0.42	0.42	0.01	0.50	31	10^7	5.0	500	13.30	13.30	13.30	0.0528
PRB	8	4	1536	768	256	0.47	0.47	0.01	0.55	31	10^7	5.0	600	12.99	12.99	13.00	0.0446
PRB	8	4	1536	768	256	0.51	0.51	0.01	0.60	32	10^7	5.0	700	12.78	12.78	12.80	0.0387
PRB	8	4	1536	768	256	0.55	0.55	0.01	0.64	32	10^7	5.0	800	12.59	12.59	12.61	0.0343
PRB	8	4	1536	768	256	0.58	0.58	0.01	0.68	32	10^7	5.0	900	12.53	12.52	12.54	0.0307
PRB	8	4	1536	768	256	0.61	0.61	0.01	0.72	32	10^7	5.0	1000	12.43	12.43	12.44	0.0278
PRB	8	4	1536	768	256	0.68	0.68	0.01	0.79	32	10^7	5.0	1200	12.34	12.34	12.34	0.0234
PRB	8	4	1536	768	256	0.79	0.79	0.01	0.92	32	10^7	5.0	1500	12.49	12.48	12.46	0.0203
PRB	8	4	1536	768	256	0.91	0.91	0.01	1.06	33	10^7	5.0	2000	12.01	11.99	11.99	0.0151
PRB	8	4	1536	768	256	1.14	1.14	0.02	1.34	31	10^7	5.0	3000	13.48	13.45	13.47	0.0107
PRB	8	4	1536	768	256	1.41	1.41	0.02	1.65	28	10^7	5.0	4000	15.62	15.55	15.60	0.00912
PRB	8	4	1536	768	256	1.71	1.71	0.02	2.00	26	10^7	5.0	5000	18.47	18.32	18.55	0.00858
PRB	8	4	1536	768	256	2.00	2.00	0.03	2.35	24	10^7	5.0	6000	21.72	21.52	21.94	0.00822
PRB	8	4	1536	768	256	2.29	2.29	0.03	2.69	22	10^7	5.0	7000	24.50	24.14	24.41	0.00791
PRB	8	4	1536	768	256	2.57	2.57	0.04	3.01	21	10^7	5.0	8000	26.90	26.39	26.97	0.00759
PRB	8	4	1536	768	256	2.84	2.84	0.04	3.33	21	10^7	5.0	9000	28.72	27.98	28.95	0.00733
PRB	8	4	1536	768	256	3.10	3.10	0.04	3.64	20	10^7	5.0	10 000	30.42	29.42	30.49	0.0071
PRB	8	4	2048	1024	384	0.04	0.04	0.00	0.04	30	10^8	1.0	10	30.73	30.75	30.76	2.17
PRB	8	4	2048	1024	384	0.14	0.14	0.00	0.15	30	10^8	1.0	20	30.85	30.86	30.97	6.35
PRB	8	4	2048	1024	384	0.13	0.13	0.00	0.14	30	10^8	1.0	30	30.78	30.78	30.86	2.55
PRB	8	4	2048	1024	384	0.16	0.16	0.00	0.17	30	10^8	1.0	40	30.98	30.98	31.04	2.16
PRB	8	4	2048	1024	384	0.19	0.19	0.00	0.20	30	10^8	1.0	50	30.92	30.92	30.90	1.89
PRB	8	4	2048	1024	384	0.18	0.18	0.00	0.19	30	10^8	1.0	60	30.76	30.78	30.83	1.19
PRB	8	4	2048	1024	384	0.21	0.21	0.00	0.22	30	10^8	1.0	70	30.87	30.87	30.86	1.22

Table 3. For caption see next page.

System	Γ_x	Γ_y	N_x	N_y	N_z	x^+	y^+	z_w^+	z_m^+	N_{BL}	Ra	Pr	Re_S	Nu_w	Nu_{ϵ_θ}	Nu_{ϵ_u}	C_S
PRB	8	4	2048	1024	384	0.23	0.23	0.00	0.24	30	10^8	1.0	80	30.72	30.72	30.77	1.11
PRB	8	4	2048	1024	384	0.25	0.25	0.00	0.27	30	10^8	1.0	90	30.69	30.70	30.73	1.05
PRB	8	4	2048	1024	384	0.21	0.21	0.00	0.22	30	10^8	1.0	100	30.93	30.92	30.89	0.562
PRB	8	4	2048	1024	384	0.32	0.32	0.00	0.33	30	10^8	1.0	200	30.85	30.85	30.83	0.329
PRB	8	4	2048	1024	384	0.42	0.42	0.00	0.44	30	10^8	1.0	300	30.81	30.81	30.84	0.254
PRB	8	4	2048	1024	384	0.47	0.47	0.00	0.49	30	10^8	1.0	400	30.69	30.68	30.61	0.184
PRB	8	4	2048	1024	384	0.53	0.53	0.00	0.55	30	10^8	1.0	500	30.78	30.80	30.78	0.147
PRB	8	4	2048	1024	384	0.58	0.58	0.00	0.61	30	10^8	1.0	600	30.75	30.75	30.82	0.123
PRB	8	4	2048	1024	384	0.63	0.63	0.01	0.66	30	10^8	1.0	700	30.72	30.73	30.69	0.107
PRB	8	4	2048	1024	384	0.68	0.68	0.01	0.71	30	10^8	1.0	800	30.58	30.59	30.57	0.0935
PRB	8	4	2048	1024	384	0.70	0.70	0.01	0.74	30	10^8	1.0	900	30.45	30.45	30.43	0.0804
PRB	8	4	2048	1024	384	0.75	0.75	0.01	0.78	31	10^8	1.0	1000	30.34	30.35	30.29	0.0731
PRB	8	4	2048	1024	384	0.85	0.85	0.01	0.89	31	10^8	1.0	1200	30.21	30.22	30.23	0.066
PRB	8	4	2048	1024	384	0.96	0.96	0.01	1.00	31	10^8	1.0	1500	30.01	30.01	29.95	0.0537
PRB	8	4	2048	1024	384	1.08	1.08	0.01	1.12	31	10^8	1.0	2000	29.33	29.32	29.38	0.0379
PRB	8	4	2048	1024	384	1.36	1.36	0.01	1.42	32	10^8	1.0	3000	27.95	27.96	27.96	0.027
PRB	8	4	2048	1024	384	1.60	1.60	0.01	1.67	33	10^8	1.0	4000	26.93	26.93	26.90	0.0211
PRB	8	4	2048	1024	384	1.81	1.81	0.02	1.89	33	10^8	1.0	5000	26.17	26.17	26.26	0.0172
PRB	8	4	2048	1024	384	2.01	2.01	0.02	2.10	33	10^8	1.0	6000	25.62	25.59	25.60	0.0147
PRB	8	4	2048	1024	384	2.18	2.18	0.02	2.28	34	10^8	1.0	7000	25.35	25.34	25.45	0.0128
PRB	8	4	2048	1024	384	2.34	2.34	0.02	2.44	34	10^8	1.0	8000	25.29	25.27	25.37	0.0112
PRB	8	4	2048	1024	384	2.51	2.51	0.02	2.62	34	10^8	1.0	9000	25.30	25.27	25.34	0.0102
PRB	8	4	2048	1024	384	2.67	2.67	0.02	2.78	33	10^8	1.0	10000	25.52	25.49	25.52	0.00931

Table 3. Simulations considered in this work. The aspect ratios of the computational domain are given by Γ_x in the streamwise direction and Γ_y in the spanwise direction. The values of N_x, N_y and N_z indicate the number of grid points in the streamwise, spanwise and wall-normal directions. The grid spacing in wall units in the streamwise and spanwise directions is given by Δx^+ and Δy^+, respectively. The wall-normal grid spacing in wall units at the wall and the mid-height are given by Δz_w^+ and Δz_c^+, respectively. The number of grid points in the wall-normal direction within the thermal BL is given by N_{BL}. Here, Nu_w indicates the value of Nusselt number computed using the average gradient of reduced temperature profile at the walls using (1.5) and Nu_{ϵ_θ} and Nu_{ϵ_u} indicate the Nusselt numbers that satisfy the global balance of thermal and kinetic dissipation (2.1) and (2.2).

REFERENCES

AHLERS, G., BODENSCHATZ, E., FUNFSCHILLING, D., GROSSMANN, S., HE, X., LOHSE, D., STEVENS, R.J.A.M. & VERZICCO, R. 2012 Logarithmic temperature profiles in turbulent Rayleigh–Bénard convection. *Phys. Rev. Lett.* **109**, 114501.

AHLERS, G., *et al*. 2022 Aspect ratio dependence of heat transfer in a cylindrical Rayleigh–Bénard cell. *Phys. Rev. Lett.* **128**, 084501.

AHLERS, G., BODENSCHATZ, E. & HE, X. 2014 Logarithmic temperature profiles of turbulent Rayleigh–Bénard convection in the classical and ultimate state for a Prandtl number of 0.8. *J. Fluid Mech.* **758**, 436–467.

AHLERS, G., GROSSMANN, S. & LOHSE, D. 2009 Heat transfer and large scale dynamics in turbulent Rayleigh–Bénard convection. *Rev. Mod. Phys.* **81**, 503–537.

BERNARDINI, M., PIROZZOLI, S., QUADRIO, M. & ORLANDI, P. 2013 Turbulent channel flow simulations in convecting reference frames. *J. Comput. Phys.* **232** (1), 1–6.

BLASIUS, H. 1908 Grenzschichten in Flüssigkeiten mit kleiner Reibung. *Z. Math. Phys.* **56**, 1–37.

BLASS, A., TABAK, P., VERZICCO, R., STEVENS, R.J.A.M. & LOHSE, D. 2021 The effect of Prandtl number on turbulent sheared thermal convection. *J. Fluid Mech.* **910**, A37.

BLASS, A., ZHU, X., VERZICCO, R., LOHSE, D. & STEVENS, R.J.A.M. 2020 Flow organization and heat transfer in turbulent wall sheared thermal convection. *J. Fluid Mech.* **897**, A22.

CHILLA, F. & SCHUMACHER, J. 2012 New perspectives in turbulent Rayleigh–Bénard convection. *Eur. Phys. J.* E **35**, 58.

DEARDORFF, J.W. 1965 Gravitational instability between horizontal plates with shear. *Phys. Fluids* **8** (6), 1027–1030.

DOMARADZKI, J.A. & METCALFE, R.W. 1988 Direct numerical simulations of the effects of shear on turbulent Rayleigh–Bénard convection. *J. Fluid Mech.* **193**, 499–531.

FUNFSCHILLING, D., BROWN, E., NIKOLAENKO, A. & AHLERS, G. 2005 Heat transport by turbulent Rayleigh–Bénard convection in cylindrical cells with aspect ratio one and larger. *J. Fluid Mech.* **536**, 145–154.

GROSSMANN, S. & LOHSE, D. 2000 Scaling in thermal convection: a unifying view. *J. Fluid Mech.* **407**, 27–56.

GROSSMANN, S. & LOHSE, D. 2001 Thermal convection for large Prandtl number. *Phys. Rev. Lett.* **86**, 3316–3319.

GROSSMANN, S. & LOHSE, D. 2002 Prandtl and Rayleigh number dependence of the Reynolds number in turbulent thermal convection. *Phys. Rev.* E **66**, 016305.

GROSSMANN, S. & LOHSE, D. 2004 Fluctuations in turbulent Rayleigh–Bénard convection: the role of plumes. *Phys. Fluids* **16**, 4462–4472.

GROSSMANN, S. & LOHSE, D. 2011 Multiple scaling in the ultimate regime of thermal convection. *Phys. Fluids* **23**, 045108.

GROSSMANN, S. & LOHSE, D. 2012 Logarithmic temperature profiles in the ultimate regime of thermal convection. *Phys. Fluids* **24**, 125103.

HARTMANN, R., YERRAGOLAM, G.S., VERZICCO, R., LOHSE, D. & STEVENS, R.J.A.M. 2023 Optimal heat transport in rotating Rayleigh–Bénard convection at large Rayleigh numbers. *Phys. Rev. Fluids* **8**, 083501.

HATHAWAY, D. & SOMERVILLE, R. 1986 Nonlinear interactions between convection, rotation and flows with vertical shear. *J. Fluid Mech.* **164**, 91–105.

HUTCHINS, N. & MARUSIC, I. 2007 Evidence of very long meandering features in the logarithmic region of turbulent boundary layers. *J. Fluid Mech.* **579**, 1–28.

INGERSOLL, A.P. 1966 Thermal convection with shear at high Rayleigh number. *J. Fluid Mech.* **25**, 209–228.

VON KÁRMÁN, T. 1934 Turbulence and skin friction. *J. Aeronaut. Sci.* **1** (1), 1–20.

KAYS, W.M. & CRAWFORD, M.E. 1993 *Convective Heat and Mass Transfer*, 3rd edn. McGraw Hill.

KERR, R. & HERRING, J.R. 2000 Prandtl number dependence of Nusselt number in direct numerical simulations. *J. Fluid Mech.* **419**, 325–344.

KOOIJ, G.L., BOTCHEV, M.A., FREDERIX, E.M.A., GEURTS, B.J., HORN, S., LOHSE, D., VAN DER POEL, E.P., SHISHKINA, O., STEVENS, R.J.A.M. & VERZICCO, R. 2018 Comparison of computational codes for direct numerical simulations of turbulent Rayleigh–Bénard convection. *Comput. Fluids* **166**, 1–8.

KRAICHNAN, R.H. 1962 Turbulent thermal convection at arbitrary Prandtl number. *Phys. Fluids* **5**, 1374–1389.

LEE, M. & MOSER, R.D. 2018 Extreme-scale motions in turbulent plane Couette flows. *J. Fluid Mech.* **842**, 128–145.

LOHSE, D. 1994 Crossover from high to low Reynolds number turbulence. *Phys. Rev. Lett.* **73**, 3223–3226.

LOHSE, D. & SHISHKINA, O. 2023 Ultimate turbulent thermal convection. *Phys. Today* **76** (11), 26–32.

Lohse, D. & Xia, K.-Q. 2010 Small-scale properties of turbulent Rayleigh–Bénard convection. *Annu. Rev. Fluid Mech.* **42**, 335–364.
Lozano-Durán, A. & Jiménez, J. 2014 Effect of the computational domain on direct simulations of turbulent channels up to $Re_\tau = 4200$. *Phys. Fluids* **26** (1), 011702.
Pirozzoli, S., Bernardini, M. & Orlandi, P. 2014 Turbulence statistics in Couette flow at high Reynolds number. *J. Fluid Mech.* **758**, 327–343.
Pirozzoli, S., Bernardini, M., Verzicco, R. & Orlandi, P. 2017 Mixed convection in turbulent channels with unstable stratification. *J. Fluid Mech.* **821**, 482–516.
van der Poel, E.P., Ostilla-Mónico, R., Donners, J. & Verzicco, R. 2015 A pencil distributed finite difference code for strongly turbulent wall-bounded flows. *Comput. Fluids* **116**, 10–16.
Prandtl, L. 1904 Über Flüssigkeitsbewegung bei sehr kleiner Reibung. In *Verhandl. III, Internat. Math.-Kong., Heidelberg* (ed. A. Krazer), pp. 484–491. B. G. Teubner Verlag.
Prandtl, L. 1932 Zur turbulenten Strömung in Rohren und längs Platten. *Ergeb. Aerodyn. Vers. Gött.* **4**, 18–29.
Quadrio, M., Frohnapfel, B. & Hasegawa, Y. 2016 Does the choice of the forcing term affect flow statistics in DNS of turbulent channel flow? *Eur. J. Mech. (*B*/Fluids)* **55**, 286–293.
Roche, P.-E. 2020 The ultimate state of convection: a unifying picture of very high Rayleigh numbers experiments. *New J. Phys.* **22** (7), 073056.
Scagliarini, A., Einarsson, H., Gylfason, A. & Toschi, F. 2015 Law of the wall in an unstably stratified turbulent channel flow. *J. Fluid Mech.* **781**, R5.
Scagliarini, A., Gylfason, A. & Toschi, F. 2014 Heat-flux scaling in turbulent Rayleigh–Bénard convection with an imposed longitudinal wind. *Phys. Rev.* E **89**, 043012.
Shevkar, P.P., Gunasegarane, G.S., Mohanan, S.K. & Puthenveetil, B.A. 2019 Effect of shear on coherent structures in turbulent convection. *Phys. Rev. Fluids* **4**, 043502.
Shishkina, O. 2021 Rayleigh–Bénard convection: the container shape matters. *Phys. Rev. Fluids* **6**, 090502.
Shishkina, O., Stevens, R.J.A.M., Grossmann, S. & Lohse, D. 2010 Boundary layer structure in turbulent thermal convection and its consequences for the required numerical resolution. *New J. Phys.* **12**, 075022.
Shraiman, B.I. & Siggia, E.D. 1990 Heat transport in high-Rayleigh number convection. *Phys. Rev.* A **42**, 3650–3653.
Siggia, E.D. 1994 High Rayleigh number convection. *Annu. Rev. Fluid Mech.* **26**, 137–168.
Solomon, T.H. & Gollub, J.P. 1990 Sheared boundary layers in turbulent Rayleigh–Bénard convection. *Phys. Rev. Lett.* **64**, 2382–2385.
Stevens, R.J.A.M., Blass, A., Zhu, X., Verzicco, R. & Lohse, D. 2018 Turbulent thermal superstructures in Rayleigh–Bénard convection. *Phys. Rev. Fluids* **3**, 041501.
Stevens, R.J.A.M., Lohse, D. & Verzicco, R. 2011 Prandtl and Rayleigh number dependence of heat transport in high Rayleigh number thermal convection. *J. Fluid Mech.* **688**, 31–43.
Stevens, R.J.A.M., van der Poel, E.P., Grossmann, S. & Lohse, D. 2013 The unifying theory of scaling in thermal convection: the updated prefactors. *J. Fluid Mech.* **730**, 295–308.
Stevens, R.J.A.M., Verzicco, R. & Lohse, D. 2010 Radial boundary layer structure and Nusselt number in Rayleigh–Bénard convection. *J. Fluid Mech.* **643**, 495–507.
Verzicco, R. & Camussi, R. 1997 Transitional regimes of low-Prandtl thermal convection in a cylindrical cell. *Phys. Fluids* **9**, 1287–1295.
Verzicco, R. & Orlandi, P. 1996 A finite-difference scheme for three-dimensional incompressible flow in cylindrical coordinates. *J. Comput. Phys.* **123**, 402–413.
Xia, K.-Q. 2013 Current trends and future directions in turbulent thermal convection. *Theor. Appl. Mech. Lett.* **3**, 052001.
Xia, K.-Q., Lam, S. & Zhou, S.Q. 2002 Heat-flux measurement in high-Prandtl-number turbulent Rayleigh–Bénard convection. *Phys. Rev. Lett.* **88**, 064501.
Yerragolam, G.S., Stevens, R.J.A.M., Verzicco, R., Lohse, D. & Shishkina, O. 2022*a* Passive scalar transport in Couette flow. *J. Fluid Mech.* **943**, A17.
Yerragolam, G.S., Verzicco, R., Lohse, D. & Stevens, R.J.A.M. 2022*b* How small-scale flow structures affect the heat transport in sheared thermal convection. *J. Fluid Mech.* **944**, A1.
Zonta, F. & Soldati, A. 2014 Effect of temperature dependent fluid properties on heat transfer in turbulent mixed convection. *Trans. ASME J. Heat Transfer* **136** (2), 022501.